Quantum ReLU activation for Convolutional Neural Networks to improve diagnosis of Parkinson's Disease and COVID-19

Luca Parisi[1,2,3*], Daniel Neagu[1], Renfei Ma[2,4], Felician Campean[1]

[1]*Faculty of Engineering & Informatics, University of Bradford, Richmond Road, Bradford, BD7 1DP, United Kingdom*
[2]*University of Auckland Rehabilitative Technologies Association (UARTA), University of Auckland, 11 Symonds Street, Auckland, 1010, New Zealand*
[3]*Parkinson's UK, 215 Vauxhall Bridge Rd, Pimlico, London SW1V 1EJ, United Kingdom*
[4]*Warshel Institute for Computational Biology, The Chinese University of Hong Kong, Shenzhen (CUHK–SZ), China*

*** Corresponding author (L. Parisi).**
E-mail address: luca.parisi@ieee.org. ***ORCID***: 0000-0002-5865-8708.

E-mail address: d.neagu@bradford.ac.uk (D. Neagu). *ORCID*: 0000-0002-7038-106X.
E-mail address: marenfei@cuhk.edu.cn (R. Ma). *ORCID*: 0000-0002-2495-4787.
E-mail address: f.campean@bradford.ac.uk (F. Campean). *ORCID*: 0000-0003-4166-8077.

Abstract — This study introduces a quantum-inspired computational paradigm to address the unresolved problem of Convolutional Neural Networks (CNNs) using the Rectified Linear Unit (ReLU) activation function (AF), i.e., the 'dying ReLU'. This problem impacts the accuracy and the reliability in image classification tasks for critical applications, such as in healthcare. The proposed approach builds on the classical ReLU and Leaky ReLU, applying the quantum principles of entanglement and superposition at a computational level to derive two novel AFs, respectively the 'Quantum ReLU' (QReLU) and the 'modified-QReLU' (m-QReLU). The proposed AFs were validated when coupled with a CNN using seven image datasets on classification tasks involving the detection of COVID-19 and Parkinson's Disease (PD). The out-of-sample/test classification accuracy and reliability (precision, recall and F1-score) of the CNN were compared against those of the same classifier when using nine classical AFs, including ReLU-based variations. Findings indicate higher accuracy and reliability for the CNN when using either QReLU or m-QReLU on five of the seven datasets evaluated. Whilst retaining the best classification accuracy and reliability for handwritten digits recognition on the MNIST dataset (ACC = 99%, F1-score = 99%), avoiding the 'dying ReLU' problem via the proposed quantum AFs improved recognition of PD-related patterns from spiral drawings with the QReLU especially, which achieved the highest classification accuracy and reliability (ACC = 92%, F1-score = 93%). Therefore, with these increased accuracy and reliability, QReLU and m-QReLU can aid critical image classification tasks, such as diagnoses of COVID-19 and PD.

Keywords *— Activation functions; ReLU; Convolutional Neural Network; Decision Support; COVID-19; Parkinson's Disease.*

1 INTRODUCTION

In Deep Learning (DL), a branch of Machine Learning (ML), Convolutional Neural Networks (CNNs) can process either two- or three-dimensional images ingested in their input layer, thus enabling them to learn from medical images in radiology, such as ionising techniques, e.g., computed tomography and X-rays, and non-ionising methods, e.g., magnetic resonance imaging (MRI) and ultrasound (US) (Ker *et al.*, 2017). The hidden layers in a CNN are called 'convolutional layers' from the 'convolutional' filters used to create feature maps from input images, which represent different features that can be extracted from them (LeCun *et al.*, 2015). Activation functions (AFs) within such hidden layers highly influence the output of CNNs and, thus, their classification performance, quantified by accuracy and reliability (sub-section 3.3), as they are applied to every neuron in those layers.

1.1. Impact of activations on medical image classification performance

Despite significant progress has been made to facilitate learning in CNNs, such as via pre-training (Hinton & Salakhutdinov, 2006), the AFs used in CNNs and related architectures have remained almost unaltered (Litjens, et al., 2017). The continued reliance on non-optimal AFs has impacted the performance of CNNs for medical diagnostic applications. This work is focused on DL-based image classification to aid medical diagnosis of COVID-19 and Parkinson's Disease (PD).

SARS-CoV-2 is responsible for COrona VIrus Disease (COVID-19), the 'severe acute respiratory syndrome coronavirus 2' (Cohen & Normile, 2020) and the current global pandemic announced by the World Health Organization (WHO, Mar 2020). This virus leads to respiratory disease in humans (Cui *et al.*, 2019), but it may take from two to fourteen days for the initial symptoms, e.g., fever and cough, to become manifest after an infection (Centers for Disease Control and Prevention, 2020). A sixteen-layered CNN model named 'POCOVID-Net' attained only recently a satisfactory performance in detecting COVID-19 from bacterial pneumonia based on pathophysiological patterns identified on US images (Born et al., 2020). However, more severe symptoms can progress to viral pneumonia, typically requiring mechanical ventilation to assist patients with breathing (Verity *et al.*, 2020). In more severe cases, COVID-19 may also lead to death (Zhou, et al., 2020), and it has been identified as one of the factors leading to the progression of PD too (Beauchamp *et al.*, 2020).

Thus, it is important to be able to detect neurodegenerative co-morbidities, such as PD, in vulnerable undiagnosed patients, promptly and non-invasively. CNNs could help to improve their clinical outcomes by aiding an earlier diagnosis of PD and COVID-19 via recognition of pathophysiological patterns from spiral drawings as indicators of PD-related tremor, and those related to the pleural thickening that is typical of COVID-19 lungs (Bhaskar *et al.*, 2020), which may be clinically misdiagnosed with viral and bacterial pneumonia (Shi *et al.*, 2020). Improvements in the AFs of CNNs can help to improve the ability to detect such pathological patterns and aid in other medical image DL-based classification tasks.

1.2. A survey on the 'dying ReLU' problem and its impact on image classification

Different layers of a CNN can capture various degrees of patterns from input images (Zeiler & Fergus, 2014). AFs provide the layers of CNNs with the gradient required to learn from non-linear data, even in the presence of noise. AFs are differentiable and can be either saturated or unsaturated. The main AFs commonly used in CNN are summarised in **Table A1** (in the Appendix), along with their equations and references.

Saturated AFs are continuous with their output threshold into finite boundaries, typically represented as S-shaped curves, also named 'sigmoidal' or 'squashing' AFs (Liew *et al.*, 2016). However, saturated AFs lead to the 'vanishing gradient' issue, whilst training a network with back-propagation (Cui, 2018), i.e., it results in gradients that are less than 1, which become smaller with multiple differentiations and ultimately zero, or 'vanish'. Moreover,

the ‘exploding gradient’ problem can occur, which has an opposite effect to that of vanishing gradients, wherein the error gradient in the weights is so high that it leads to instability during back-propagation. The hyperbolic tangent or ‘tanh’ (**Table A1** in the Appendix) is another saturated AF, which attempts to mitigate this issue by extending the range of the sigmoid or logistic function from [0, 1] to [-1, 1], centred at 0. Nevertheless, *tanh* does not solve the ‘vanishing gradient’ problem.

Unsaturated functions are not bounded in any output ranges and are centred at 0. The Rectified Linear Unit (ReLu) (**Table A1** in the Appendix) is the most widely applied unsaturated AF in CNNs, which provides faster convergence than the sigmoid (LeCun *et al.*, 1998) and *tanh* AFs, as well as improved accuracy (Litjens *et al.*, 2017). In fact, ReLU generally leads to more efficient updates of weights during back-propagation (Gao *et al.*, 2020). The ReLU’s gradient is either one for zero and positive inputs or zero for negative ones (**Table A1** in the Appendix), thus solving the ‘vanishing gradient’ issue. However, despite providing appropriately small random values to the weights in their initialisation stage (Glorot *et al.*, 2011), with large weight updates, the summed input to the ReLU is always negative (‘dying ReLU’ problem). This issue results in a zero value at the output and the corresponding nodes do not have any influence on the network (Abdelhafiz *et al.*, 2019), thus hindering generalisation in critical image ML-aided classification tasks, such as those in healthcare, e.g., COVID-19 or PD diagnostics.

To mitigate the ‘dying ReLU’ problem, in CNNs, whilst leveraging classical computational approaches, multiple variations of the ReLU have been introduced, such as the Leaky ReLU (LReLU), the Parametric ReLU (PReLU), the Randomised ReLU (RReLU), and the Concatenated ReLU (CReLU), as summarised in **Table A1** in the Appendix. Maas *et al.* (2013) introduced the LReLU to provide a small negative gradient for negative inputs into a ReLU function, instead of being 0. A constant variable α, with a value of 0.01, was used to compute the output for negative inputs (**Table A1** in the Appendix). LReLU is implemented in the two most widely used Python open-source libraries for DL named ‘TensorFlow’ and ‘Keras’ with the default values of α set to 0.2 and 0.3 respectively ((TensorFlow Core v2.3.0: tf.nn.leaky_relu, 30) and (TensorFlow Core v2.3.0: tf.keras.layers.LeakyReLU, 30)). Via this modification, LReLU leads to small improvements in overall classification performance as compared to the ReLU.

Another variant of the ReLU, named ‘Exponential Linear Unit’ (ELU), slightly improves its convergence (Maas *et al.*, 2013) (**Table A1** in the Appendix), but it does not solve the ‘dying ReLU’ issue. Klambauer *et al.* (2017) introduced a variant of the ELU called ‘Scaled Exponential linear Unit’ (SELU) (**Table A1** in the Appendix), which is a self-normalising function that provides an output normal distribution graph, making it suitable for CNN with the output converging to zero mean. Although the SELU attempts to avoid both vanishing and exploding gradient problems, it does not resolve the ‘dying ReLU’ issue either.

He *et al.* (2015) proposed the PReLU to provide a better performance than the ReLU in large-scale image classification tasks, although the only difference with respect to the LReLU lies in α varying during back-propagation. Nevertheless, due to this mechanism, the PReLU does not solve the ‘dying ReLU’ issue either, as it is another slight and classical variation of the LReLU. Similarly, the RReLU is a classical version of LReLU (Pedamonti,

2018), whereby α is a random number sampled from a uniform distribution, thus being still subject to the 'dying ReLU' issue. Shang *et al.* (2016) proposed a further slight improvement to the ReLU named 'Concatenated ReLU' (CReLU), allowing for both positive and negative input activations, by applying ReLU after copying the input activations and concatenating them. Thus, CReLU is computationally more expensive and still prone to the 'dying ReLU' problem, although it generally leads to competitive classification performance with respect to the gold standard ReLU and LReLU (Shang *et al.*, 2016).

In summary, despite the wide application of CNNs for image classification in healthcare, the issue of 'dying ReLU' is still a major challenge affecting the reliability of DL-based algorithms in critical image classification tasks. As discussed, none of the recently proposed AFs described above, including the most common and reliable one in CNNs, i.e., the LReLU, have effectively addressed this issue yet, as their approaches are still classical algorithmically and very similar to the ReLU.

This issue can impact the classification performance of CNNs in a clinical setting. For example, considering the CNN of Kollias *et al.* (2018), the last fully connected layer with 1,500 neurons had only 30 of them yielding non-zero values, due to the 'dying ReLU' problem. Even by having the last dense layer with 128 neurons (Kollias *et al.*, 2018), only 20 of them led to non-zero output values, whilst the remaining ones experienced the 'dying ReLU' issue, thus yielding negligible values. These examples provide empirical evidence that classical approaches to ReLU failed to solve its associated 'dying ReLU' problem. Thus, in this study, an alternative approach leveraging quantum-inspired computation is proposed to address this issue, with related studies in sub-section 1.3 and this study's contributions outlined in sub-section 1.4.

1.3. Related literature and limitations with Quantum Machine Learning approaches

Quantum ML is a relatively new field that blends the computational advantages brought by quantum computing and advances in ML beyond classical computation (Ciliberto, et al., 2018). When run on quantum hardware, Quantum ML has not only led to a lower computational cost with respect to classical algorithms, but it has also enabled to find the global *minimum* in the solutions sought after in ML with a higher probability (Ciliberto, et al., 2018). The main principles of quantum computing are those inherited from quantum physics, such as superposition and entanglement (Barabasi *et al.*, 2019). According to the principle of superposition, the fundamental quantum bit or 'qubit' can have multiple states at any point in time, i.e., a qubit can have a value of either 0 or 1, such as classical bits, but, differently from and beyond classical bits, a qubit can also have both values 0 and 1 concurrently (Barabasi *et al.*, 2019). A quantum gate is the unification of two quantum states 'entangled' into one, wherein a change in a state can affect the other one and vice versa (Jozsa & Linden, 2003). Thus, a system of qubits, each of which holding multiple bits of information concurrently, behaves as one via 'entanglement', thus facilitating parallelism (Cleve *et al.*, 1998; Schuld *et al.*, 2014; Solenov *et al.*, 2018).

However, existing quantum approaches to implement AFs in CNNs have only adopted the repeat-until-success (RUS) technique to achieve pseudo non-linearity due to restrictions to linear and unitary operations in quantum mechanics (Nielsen & Chuang, 2002; Cao *et al.*, 2017). This RUS approach to AFs involves an individual state preparation and the generation of superimposed and entangled linear combinations to propagate the routine of an AF to all states in unison. Thus, a CNN leveraging this quantum RUS technique could theoretically approximate most non-linear AFs (Macaluso *et al.*, 2020). Nevertheless, the practical applications of this approach are very limited due to the input range of the neurons in such architectures being bounded between 0 and $\pi/2$ as a trade-off of their theoretically generic AF formulation. Hu (2018) led a similar theoretical research effort in proposing a sigmoid-based non-linear AF, which is not periodic, to enable a more efficient gradient descent whilst leveraging the principle of superposition in training neurons with multiple states concurrently. However, the classical form of the approach of Hu (2018) is the traditional ReLU, thus still not solving the 'dying ReLU' problem. Konarac *et al.* (2020) leveraged a similar quantum-based sigmoid AF in their Quantum-Inspired Self-Supervised Network (QIS-Net) to provide high accuracy (99%) and sensitivity (96.1%) in the segmentation of MRI images, improving accuracy and reliability by about 1% with respect to classical approaches.

As described in sub-sections 1.1 and 1.2, CNNs are highly suitable in classifying medical images due to their intrinsic feature extraction mechanisms. As illustrated in both 1.2 and this sub-section (1.3), the importance of the AF is evident in both classical and quantum DL. Although numerous classical computational variants of ReLU functions have been proposed in CNNs (sub-section 1.2), they have not been widely adopted as ReLU and LReLU. These two AFs typically ensure accurate and reliable classification; moreover, they are readily available in TensorFlow and Keras. Nevertheless, these AFs and any other recent AFs (sub-section 1.2) have not solved the 'dying ReLU' problem yet, as they leveraged classical approaches instead, which still allow for small negative values (e.g., LReLU; **Table A1** in the Appendix). Moreover, vanishing and exploding gradient issues have not been fully resolved either (sub-section 1.2). At times, ELU and SELU (**Table A1** in the Appendix) may provide faster convergence than ReLU and LReLU, but they are not as reliable as those and are computationally more expensive (Pedamonti, 2018).

1.4. Proposed quantum computational approach and contributions

In this study, the proposed approach is underpinned by the realisation whereby the two quantum properties of entanglement and superposition can be pivotal in solving the 'dying ReLU' problem via quantum computation. By building on the LReLU that mitigates the 'dying ReLU' problem and further to applying both these quantum principles on it, two novel AFs are derived to leverage such quantum computations to avoid a negative solution by preferring the positive one. This contrasts with traditional classical ReLU that may fail by leading to negative solutions only.

The unresolved issues with ReLU-based AFs (sub-section 1.2) and current quantum methods (sub-section 1.3) impact the diagnostic accuracy and reliability (sub-section 3.3) of an application leveraging CNNs for aiding detection of COVID-19 or PD in a clinical setting. Such an impact can be quantified by a higher number of false negatives, when the model accuracy and reliability (sub-section 3.3) are evaluated on unseen patient data. The authors have hypothesised that these impaired accuracy and reliability are due to the classical approach underpinning such ReLU-based AFs that have been just moulded in various ways so far, retaining the inherent functional limitations of the classical ReLU.

Conversely, this study's main novelties and contributions are as follows:

- Theoretical advancement: Proposing to leverage a quantum-based computational approach to solve the 'dying ReLU' issue, instead of classical ReLU-like approaches as those reviewed in sub-section 1.2 that failed to solve this problem, thus avoiding negative states of the values input to the AF.
- Practical impact: Differently from classical methods that allow for small negative values, such as the LReLU, the proposed quantum-inspired paradigm can improve the accuracy and the reliability of CNNs in aiding critical medical image diagnostics.

By blending the two key quantum principles of entanglement and superposition to help in reaching the global *minimum* in the solution, thus avoiding negative solutions differently from classical approaches as in sub-section 1.2, this study investigates the development of two novel AFs, the 'Quantum ReLU' (QReLU) and the 'modified Quantum ReLU' (m-QReLU), to avoid the problem of the 'dying ReLU' in a quantistic manner. This builds on recent research efforts by Cong *et al.* (2019) to develop a Quantum CNN, which showed how quantum states can be embedded in such a DL architecture, by extending this principle from a high-level architectural standpoint down to the level of AFs, thus addressing the inherent 'dying ReLU' problem.

Patterns from US images of lungs and spiral drawings as indicators of pleural thickening and deviations from physiological tremor are known diagnostic biomarkers for COVID-19 and PD respectively, with PD being at times a delicate neurodegenerative co-morbidity of patients with COVID-19. Improvements in accuracy and reliability (sub-section 3.3) are key to aid early diagnosis that can improve outcomes, especially in the event of such co-morbidities. Thus, the novel QReLU and m-QReLU were leveraged in a CNN to improve its classification accuracy and reliability (sub-section 3.3) in these pattern recognition tasks, as quantified via clinically relevant and interpretable metrics, and compared against the same CNN with current gold-standard AFs, including the ReLU and the LReLU. The proposed added quantum computational capability of QReLU and m-QReLU in a CNN was hypothesised to improve its accuracy and reliability (sub-section 3.3) for pattern recognition in image classification for critical applications, such as in healthcare involving medical image diagnostics, e.g., detecting COVID-19 and PD from non-invasive, relatively inexpensive, and portable methods, such as US scans and graphic tablets to draw spiral drawings on, respectively.

The remaining sections of the paper are structured as follows. **Section 2** deals with the theory/calculation, including sub-section 2.1 illustrating the two novel quantum AFs, along with their mathematical formulation and respective implementations in both TensorFlow and Keras. Sub-section 2.2 provides an interpretation and the expected impact of the proposed quantum activations. **Section 3** provides a description of the methods used, including the hardware and software resources in sub-section 3.1, the AFs and a description of the datasets selected for validation, along with a standardised data pre-processing strategy (sub-section 3.2), and the classification accuracy and reliability metrics assessed (sub-section 3.3). **Section 4** summarises the results obtained comparing the accuracy, reliability, and computational time of a CNN with the proposed quantum AFs against salient gold standard AFs outlined in **Table A1** in the Appendix. The 'computational time' shown on **Tables A2-A8** (Tables A2, A3, A6, A7, and A8 are in the Appendix) includes both the training and evaluation time. Eventually, **section 5** provides a thorough discussion of the results and **section 6** summarises the current work and outlines its access, impact, and future applications.

2 THEORY/CALCULATION

In this section, two new AFs leveraging quantum computation are explicitly defined, including both their mathematical equations that describe them and their corresponding algorithmic implementations in industry-standard Python libraries for DL, i.e., TensorFlow and Keras. Furthermore, these novel quantum-inspired activation functions are explained, along with the impact expected of them.

2.1. Proposed quantum activation functions

A multi-step quantum approach (**Fig. 1**) was applied to ReLU first, by selecting its solution for positive values ($\mathrm{R(z)}_{\mathrm{ReLU}} = z, \forall\, z > 0$), and the LReLU's solution for negative values ($\mathrm{R(z)}_{\mathrm{LReLU}} = \alpha \times z$, $\forall\, z \leq 0, where\ \alpha = 0.01$) as a starting point to improve quantistically.

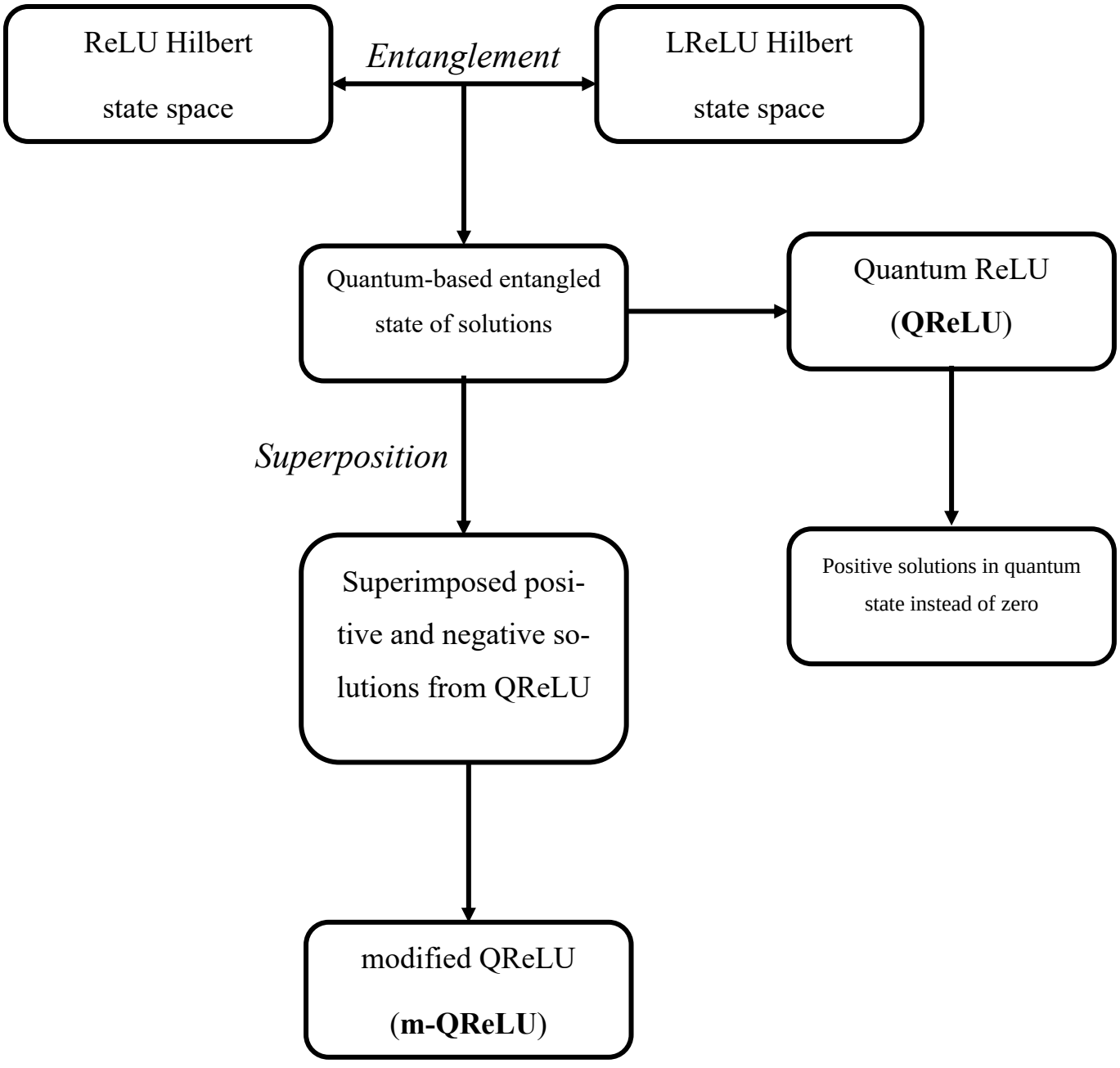

Figure 1. A flowchart illustrating the quantum-inspired paradigm that led to the derivation of the Quantum ReLU (QReLU) and the modified QReLU (m-QReLU) activation functions.

By applying the quantum principle of entanglement, the tensor product of the two candidate Hilbert state spaces from ReLU (H_{ReLU}) and LReLU (H_{LReLU}) was performed, as per formula (1):

$$H_{ReLU} \otimes H_{LReLU} \quad (1)$$

The quantum entanglement in (1) allows to overcome the limitation of the ReLU being 'dying' for negative inputs, only partly obviated by the LReLU with a negligibly negative gradient instead, as over 0 or negative solution states, the positive solution states would be preferred. In fact, whilst the output from ReLU and LReLU for negative solutions would not vary or differ only negligibly respectively, which lead to misclassification and limited generalisation for data classification, the quantum entangled approach would allow for a larger variation. This is achieved by prescribing an appropriate gradient derived from preferring positive solution states instead of zero and negative ones for the ReLU and LReLU correspondingly. Therefore, if the first Hilbert ReLU-based system were in state $|\varphi\rangle_{ReLU}$ and the second Hilbert LReLU-based system were in state $|\varphi\rangle_{LReLU}$, the resulting state in the blended system would be described by formula (2):

$$|\varphi\rangle_{ReLU} \otimes |\varphi\rangle_{LReLU} \quad (2)$$

In an entangled or inseparable state, the formulation of such product states can be generalized as per equation (3):

$$|\varphi\rangle_{QReLU} = \sum_{ReLU,LReLU} k_{ReLU,LReLU} |0|1\rangle_{ReLU} \otimes |0|1\rangle_{LReLU} \quad (3)$$

Thus, the following quantum-based entangled state of solutions was obtained, as represented in (4):

$$|1\rangle_{LReLU} \otimes |0\rangle_{ReLU} - 2|0\rangle_{ReLU} \otimes |1\rangle_{LReLU} \quad (4)$$

Which, in classical form, leads to the following derivation as per equation (5):

$$R(z)_{QReLU} = \alpha \times z - 2z, \forall z \leq 0 \quad (5)$$

Thus, keeping R(z) = z for positive values (z > 0) as in the ReLU, but with the added novelty of the entangled solution for negative values (as per equations 3 and 4), the QReLU was defined as per equation (5) (**Fig. 2**). This avoids the 'dying ReLU' by maintaining the positivity of the solution via this new quantum state. The QReLU and the m-QReLU AFs have been made freely available in TensorFlow and Keras on GitHub (Parisi, 2020).

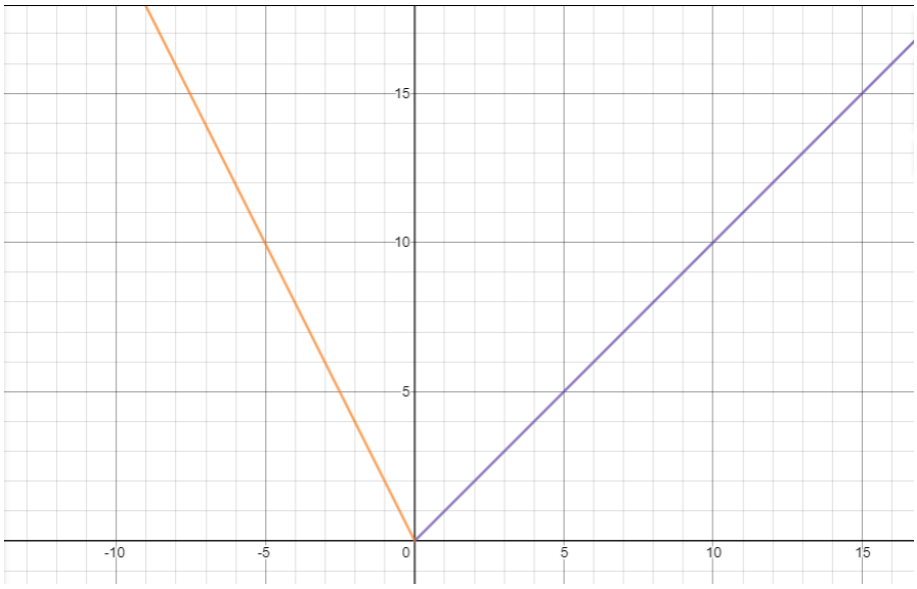

Figure 2. The Quantum ReLU (QReLU) activation function.

Whilst QReLU is a quantum-inspired entangled improvement that is built on ReLU and LReLU to solve the 'dying' ReLU problem by preferring positive solution states over negative ones or zero, as an alternative approach, quantum superposition can be further applied on top of it, such that the two solution states co-exist and the activation function can generalise further in presence of ill-behaved classical inputs, such as noisy image data. Thus, by leveraging the quantum principle of superposition on the QReLU's solution for positive and negative values, the following m-QReLU was defined in quantum computation, or, equivalently for further explainability, in classical derivation, as per equations (6) and (7), also illustrated in **Fig. 3**. The 'dying ReLU' issue is again avoided, and this implementation is made available in both TensorFlow and Keras.

$$|\varphi\rangle_{m-QReLU} = \sum_{ReLU,LReLU} k_{ReLU,LReLU} |\varphi_{ReLU,LReLU}\rangle \quad (6)$$

$$R(z)_{m-QReLU} = \alpha \times z - 2z + z = \alpha \times z - z, \forall z \leq 0 \quad (7)$$

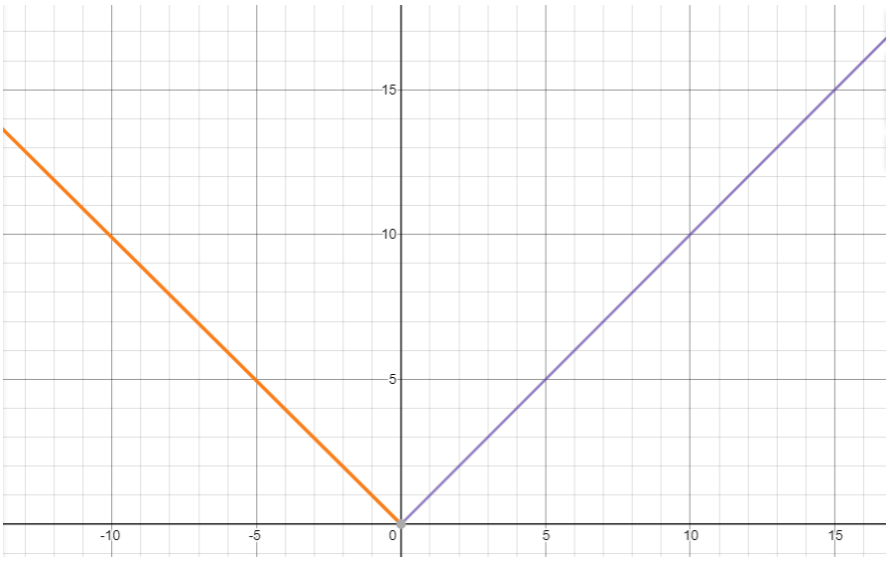

Figure 3. The modified Quantum ReLU (m-QReLU) activation function.

2.2. Interpretation and expected impact of proposed quantum activations

The m-QReLU also satisfies the entanglement principle derived via the tensor outer product of the solutions from the QReLU. Thus, a quantum-based blend of both superposition and entanglement principles computationally leads the QReLU and the m-QReLU to obviate the 'dying ReLU' problem. As shown in equations (5) and (7), by selecting the positive quantum state of the summed input of the QReLU and m-QReLU, an optimal early diagnosis could be achieved for patients with COVID-19 and PD. Thus, this study demonstrates the QReLU and m-QReLU as potential new benchmark AFs in CNNs for critical image classification tasks, particularly useful in medical diagnoses, wherein accuracy and reliability (sub-section 3.3) are key to improve patient outcomes.

To address the specific needs to improve diagnosis of PD and that of COVID-19 dealt with in this study, further datasets were used, as per the classification pipeline shown in **Fig. 4**, involving the use of US scans and spiral drawings to detect COVID-19 and PD from their patterns respectively (two sample images from the input data are shown on the two circles on the left), following appropriate data pre-processing (randomisation and normalisation). As described in sub-section 2.1, by leveraging the principles of superposition and entanglement, and building on the ReLU (red circle to indicate 'dying ReLU' problem; **Fig. 4**) and LReLU (light red circle to indicate it only mitigates the 'dying ReLU' issue, but does not solve it; **Fig. 4**), two novel quantum activations, QReLU and m-QReLU (both in green and in the middle for a better/more balanced gradient for learning; **Fig. 4**), were derived. QReLU and m-QReLU solved the 'dying ReLU' problem and enabled a CNN model to classify such images and generalise in the detection of COVID-19 and PD. $f(x)$ in **Fig. 4** represents the intermediate output obtained from the convolutional layer wherein such AFs are used, whilst W_x (**Fig. 4**) represent how the weights

of the CNN vary along the gradient based on *x*, the input data, and AF used. The circles on the right of **Fig. 4** regarding COVID-19 and spiral drawings represent clinical patterns associated with ML-based patterns leveraged by the CNN classifier to detect COVID-19 and PD, such as the pleural thickening as an imaging-based biomarker associated with for COVID-19, hence the red arrows drawn on **Fig. 4**, and the areas under the curves highlighted in red (**Fig. 4**) to indicate how clinicians currently analyse images of spiral drawings, i.e., analysing the extent of deviation from the spiral that was meant to be drawn on by the subject.

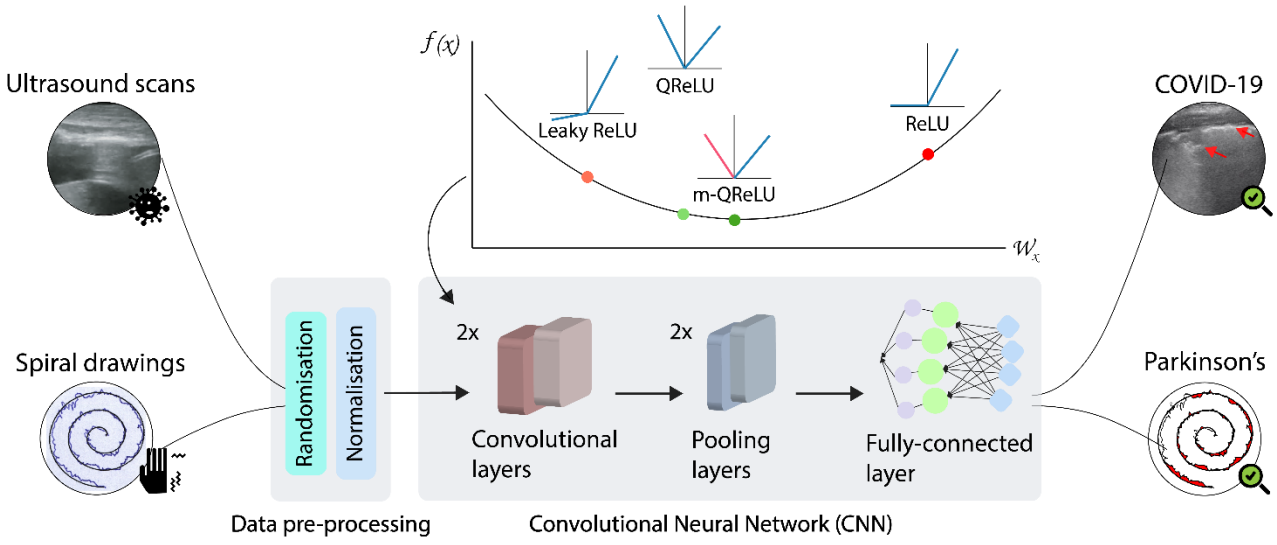

Figure 4. The classification pipeline devised and leveraged in this study, including the novel QReLU and m-QReLU that avoid the 'dying ReLU' problem, to aid detection of COVID-19 and Parkinson's Disease from ultrasound scans and images of spiral drawings, respectively.

3 METHODS

In this section, the methods used in this study have been outlined, describing the hardware and software resources and their specifications. Furthermore, to enable reproducibility of the results attained, this section includes the CNN model's hyperparameters, the AFs used for comparison, and the datasets leveraged, as well as the pipeline whereby they were pre-processed. The performance metrics used to quantify both the classification accuracy and the reliability are also provided, along with their motivation and mathematical representation where required.

3.1. Hardware and software resources

Although the two proposed AFs are quantistic in nature, both QReLU and m-QReLU can be run on classical hardware, such as central processing unit (CPU), graphics processing unit (GPU) and tensor processing unit (TPU). The latter is the type of runtime used in this study via Google Colab (http://colab.research.google.com/) to perform the required evaluation on the datasets described in 2.1. The novel QReLU and m-QReLU were developed and tested using Python 3.6 and written to be compatible with both TensorFlow (1.12 and 1.15 tested, 1.15 supports TensorFlow serving to deploy the novel AFs on the cloud) and the Keras Sequential API. Thus, both AFs were programmed as new Keras layers for ease of use. To facilitate repeatability and reproducibility, the codes of the QReLU and m-QReLU in TensorFlow and Keras have been made freely available on GitHub (Parisi, 2020). MATLAB (R2017b; Natick, The MathWorks, Inc.) was used to produce Figs. 4 and 5 only.

3.2. Activation functions and datasets for validation

Using the same standard CNN (LeCun *et al.*, 1998) with two convolutional layers (32 and 64 filters respectively, kernel size 5x5), and with one max-pooling layer after each convolutional layer and 1,024 neurons in the third fully-connected layer (**Fig. 4**), in TensorFlow for MNIST data classification, after identifying the main reproducible (with associated codes available in TensorFlow and Keras) AFs following the critical review of the literature (sub-section 1.2), the following nine classical AFs were considered: ReLU, LReLU, CReLU, sigmoid, tanh, softmax, Very LReLU (VLReLU), ELU and SELU. In all experiments, to enable a fair comparison of performance regardless of the AF leveraged, a batch size equal to 128 and maximum number of epochs of 2,000 were used (LeCun *et al.*, 1998), unless otherwise stated as per Tables A3 and A7 in the Appendix, wherein further evaluation to assess the reliability of the AFs tested, including the two proposed quantum-inspired ones, was performed by varying batch size (as 64) or the maximum number of epochs (as 1,500). k-fold (with k = 5) cross-validation was leveraged for model training to prevent overfitting (Kohavi, 1995).

To enable repeatability and reproducibility of the results obtained, publicly available datasets were gathered and used in this study, as mentioned below.

As a general benchmark dataset for any image classifiers, especially CNNs, the MNIST data (LeCun *et al.*, 1998), including 60,000 images of handwritten digits (50,000 images for training, 10,000 images for testing), was used for the initial model and AF validation. This dataset is in tensor format and available in TensorFlow (https://www.tensorflow.org/datasets/catalog/mnist).

Four datasets were leveraged to identify PD based on patterns on spiral drawings (1290 subjects in total), whilst two datasets were used to detect COVID-19 from US scans, as follows:

1. University of California Irvine (UCI) Spiral Drawings dataset (data format: .jpg; Sakar *et al.*, 2013; Isenkul *et al.*, 2014) on 77 subjects (62 PD patients, 15 healthy controls) from the Department of Neurology in Cerrahpasa Faculty of Medicine, Istanbul University.
2. Kaggle Spiral Drawings dataset (data format: .png; Zham *et al.*, 2017) on 55 subjects (27 PD patients, 28 healthy controls) from Dandenong Neurology, Melbourne, VIC, Australia.
3. Spiral HandPD dataset (data format: .jpg; Pereira *et al.*, 2016a) on 92 subjects (74 PD patients, 18 healthy controls) from the Botucatu Medical School, São Paulo State University in Brazil.
4. NewHandPD dataset (data format: .jpg; Pereira *et al.*, 2016b) on 66 additional subjects (31 PD patients, 35 healthy controls) – different from those in the 'Spiral HandPD dataset', from the Botucatu Medical School, São Paulo State University.
5. Point-of-care lung US (POCUS) images (data format: .png) were considered to detect COVID-19, including the 'COVID-19 Ultrasound' dataset with US images from the GitHub repository of Born (2020) before July 22nd, 2020.
6. POCUS 19 dataset having images from the GitHub repository of Born (2020) since July 22nd, 2020, consisting in total of 1,108 images (659 on patients with COVID-19, 277 on patients with bacterial pneumonia and 175 on healthy lungs).

As in the MNIST dataset, images in all datasets were converted to grayscale and resized to be 28*28.

3.3. Classification accuracy and reliability metrics used for evaluation

To assess which AF was suitable for each of the pattern recognition tasks involved in classifying the seven datasets as per sub-section 2.1, the accuracy of the CNN was assessed via the test or out-of-sample classification accuracy (equation (8)), whilst the reliability (Hripcsak and Rothschild, 2005) of the classification outcomes was quantified via the following metrics: precision (equation (9)), sensitivity/recall (equation (10)), and F-measure or F1-score (equation (11)), which is the harmonic mean between precision and recall. 95% confidence intervals (CIs) were also reported in all tabulated results.

The above-mentioned metrics were calculated based on the classification outcomes as per equations (8-11) below, which can be either true or false, thus resulting in one main result for each subject out of four potential ones, such as 'True Positive' (TP), 'False Positive' (FP), 'True Negative' (TN), and 'False Negative' (FN). Furthermore, in the Appendix, in support of these metrics (Hripcsak and Rothschild, 2005), the area under the receiver operating characteristic (ROC-AUC) curve (True Positive Rate (TPR) or sensitivity vs False Positive Rate (FPR) or (1-specificity)) was also computed for Tables A3 and A7, with three representatives ROC curves illustrated in Figs. 7A-9A.

$$Accuracy = \frac{TP+TN}{TP+TN+FP+FN} \quad (8)$$

$$Precision = \frac{TP}{TP+FP} \quad (9)$$

$$Recall\ or\ Sensitivity = \frac{TP}{TP+FN} \quad (10)$$

$$F1\text{-}score = 2 \times \frac{Precision \times Recall}{Precision+Recall} = \frac{TP}{TP + \frac{FP+FN}{2}} \quad (11)$$

4 RESULTS

F1-score

The CNN, designed as an MNIST classifier, was initially validated on the MNIST benchmark dataset itself, used for recognising handwritten digits. The QReLU and the m-QReLU were the best and second-best performing AFs respectively, leading to an ACC and an F1-score of 0.99 (99%) and of 0.98 (98%) respectively (**Table A2** in the Appendix). The ReLU, the LReLU and the VLReLU also led to achieve the best classification accuracy and reliability (sub-section 3.3) on the MNIST data (ACC = 0.99/99%, F1-score = 0.99/99%) (**Table A2** in the Appendix). Thus, the proposed QReLU achieved gold standard classification accuracy and reliability (sub-section 3.3) on this benchmark dataset.

Noteworthy, the QReLU and the m-QReLU led the same CNN architecture to achieve the best (ACC = 0.92/92%, F1-score = 0.93/93%) and third (ACC = 0.88/88%, F1-score = 0.90/90%) classification accuracy and reliability (**Table A3** in the Appendix and **Fig. 5**, as well as Figs. 7A and 8A in the Appendix) on the dataset named 'Spiral HandPD' on images of spiral drawings taken via graphic tablets from patients with PD and healthy subjects.

As illustrated in **Table 4**, competitive results were achieved by the QReLU and the m-QReLU versions on a further dataset on spiral drawings, the 'NewHandPD dataset', leading to the sixth and eight classification accuracy and reliability respectively (ACC = 0.83/83%, F1-score = 0.83/83%; ACC = 0.79/79%, F1-score = 0.79/79%). Very competitive outcomes were obtained by the two proposed quantum AFs on the Kaggle Spiral Drawings dataset, with m-QReLU (ACC = 0.73/73%, F1-score = 0.70/70%) and QReLU (ACC = 0.67/67%, F1-score = 0.67/67%) leading to the second and fourth classification accuracy and reliability respectively (**Table 5**), as well as when evaluated against the UCI Spiral Drawings dataset (QReLU ranked fifth with ACC = 0.82/82% and F1-score = 0.74/74%; m-QReLU ranked sixth with ACC = 0.78/78% and F1-score = 0.68/68%) (**Table A6** in the Appendix).

The overall increased accuracy and reliability (sub-section 3.3) brought about by the two novel quantum AFs is evident in the outstanding and mutually consistent classification outcomes achieved on both lung US datasets to

distinguish COVID-19 from both pneumonia and healthy subjects with the best (**Table A7** in the Appendix and **Fig. 6** - QReLU and m-QReLU with ACC = 0.73/73% and F1-score = 0.73/73%) and the second (**Table A8** in the Appendix - QReLU and m-QReLU with ACC = 0.6/60% and F1-score = 0.63/63%) classification accuracy and reliability (sub-section 3.3) respectively for both QReLU and m-QReLU.

Despite a higher computational cost (four-fold with respect to the other AFs except for the CReLU where the increase was three-fold), the results obtained by leveraging either or both the proposed QReLU and m-ReLU AFs, assessed based on classification accuracy, precision, recall and F1-score, indicate overall higher accuracy and reliability (sub-section 3.3) achieved on five of the seven datasets (**Table A2** in the Appendix on the MNIST data, **Tables A3** (in the Appendix) and **5** on PD-related spiral drawings, **Tables A7** and **A8** in the Appendix on COVID-19 lung US images). Overall, the QReLU and the m-QReLU methods are the best performing AFs that can be applied for aiding diagnosis of both COVID-19 from lung US data and PD from spiral drawings.

Specifically, when using the novel quantum AFs (QReLU and m-QReLU) as compared to the traditional ReLU and the LReLU AFs, the gold standard AFs in DNNs, the following percentage increases in ACC, precision, recall/sensitivity, and F1-score were noted:

- An increase of 55.32% in ACC and sensitivity/recall via m-QReLU as compared to ReLU and by 37.74% with respect to LReLU, thus avoiding the 'dying ReLU' problem when the CNN was evaluated on the Kaggle Spiral Drawings dataset (**Table 5**).
- An increase by 82,000% in ACC and sensitivity/recall via QReLU (82%) when compared to tanh (0% ACC and sensitivity/recall), thus avoiding the vanishing gradient problem too, as assessed on the UCI Spiral Drawings dataset (**Table A6** in the Appendix).
- An increase by 65.91% in F1-score via both QReLU and m-QReLU as opposed to LReLU, hence obviating the 'dying ReLU' problem again but when tested on the COVID-19 Ultrasound dataset (**Table A7** in the Appendix and **Fig. 6**, as well as Fig. 9A in the Appendix).
- An increase of 50% in ACC and sensitivity/recall via both QReLU and m-QReLU with regards to both ReLU and LReLU, hence solving the 'dying ReLU' problem when evaluated on the POCUS 19 Ultrasound dataset (**Table A8** in the Appendix).

Furthermore, it is worth noting the proposed quantum AFs led to improved classification outcomes as compared to recent advances in ReLU AFs, such as CReLU and VLReLU:

- QReLU led to ACC, precision, sensitivity/recall, and F1-score all higher by 1% those obtained via CReLU when evaluating the CNN's classification accuracy and reliability (sub-section 3.3) on the MNIST data (**Table A2** in the Appendix).
- m-QReLU resulted in an ACC and a sensitivity/recall higher by 3% than CReLU, and an F1-score greater by 2% on the Spiral HandPD dataset (**Table A3** in the Appendix and **Fig. 5**).

- m-QReLU led to an ACC and a sensitivity/recall greater by 11% than VLReLU, and an F1-score also higher by 11% on the Spiral HandPD dataset (**Table A3** in the Appendix and **Fig. 5**).
- m-QReLU resulted in an ACC and a sensitivity/recall higher by 6% than VLReLU, and an F1-score greater by 3% on the Kaggle Spiral Drawings dataset (**Table 5**).
- QReLU and m-QReLU led to an ACC and a sensitivity/recall greater by 9% and 18% than CReLU and VLReLU respectively, and an F1-score higher by 5% and 14% on the COVID-19 Ultrasound dataset (**Table A7** in the Appendix and **Fig. 6**).
- QReLU and m-QReLU resulted in an ACC and a sensitivity/recall higher by 20% than VLReLU, and an F1-score greater by 10% on the POCUS 19 Ultrasound dataset (**Table A8** in the Appendix).

The results obtained via the QReLU and m-QReLU in a CNN on the MNIST dataset (**Table A2** in the Appendix) are comparable to those achieved on three- (LeCun *et al.*, 1998; Siddique *et al.*, 2019; Ahlawat *et al.*, 2020) and four-layered CNNs (Siddique *et al.*, 2019; Ahlawat *et al.*, 2020), as well as deeper CNN architectures (Chen *et al.*, 2018).

The CNN's classification accuracy and reliability (sub-section 3.3) via the proposed m-QReLU (ACC = 92%, F1-score = 93%) is illustrated in **Fig. 5**, showing that the m-QReLU leads to the best classification (the top-left corner of the plot), whilst the one yielding the worst classification (VLReLU) is at the bottom-right corner; full results shown in **Table A3** in the Appendix, also including the confidence intervals for the classification performance metrics mentioned in sub-section 3.3 for all AFs). This was also higher by over 2% than the best performing five-layered CNNs (Pereira *et al.*, 2016c), to aid diagnosis of PD from spiral drawings, such as using the 'Spiral HandPD' dataset.

Similarly, a comparable precision was achieved by the CNN model (**Table A7** in the Appendix and **Fig. 6**) when the QReLU and m-QReLU were used as AFs with respect to the best classifier so far on the COVID 19 Ultrasound dataset, i.e., the sixteen-layered CNN model named ‘POCOVID-Net model’, mentioned earlier in section 1.1 (Born *et al.*, 2020).

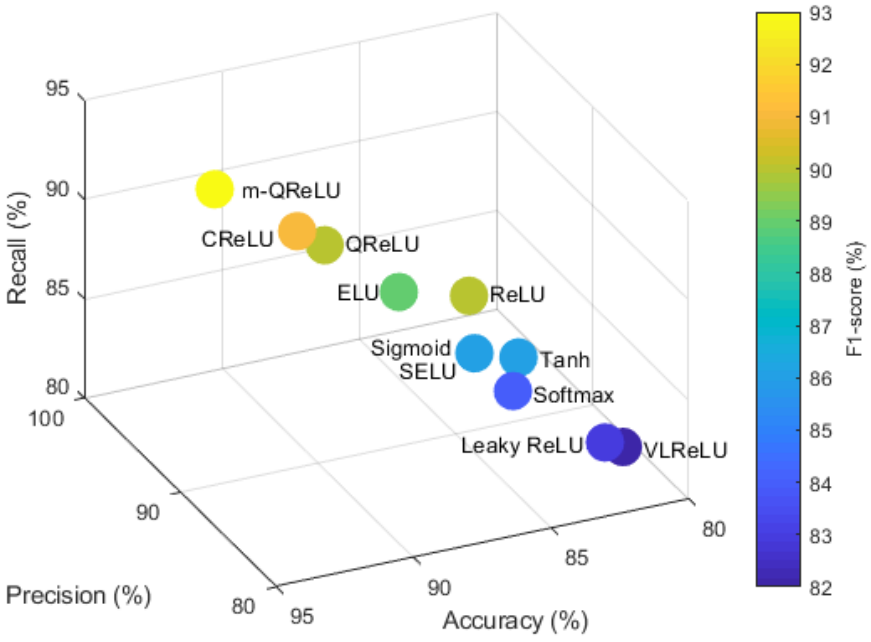

Figure 5. The classification accuracy and reliability (sub-section 3.3) of the Convolutional Neural Network on the ***Spiral HandPD dataset***, considering the main four metrics (sub-section 3.3) leveraged in percentages (%), i.e., accuracy, precision, recall, and F1-score. *Table A3* in the Appendix also includes the confidence intervals of such metrics for all AFs.

Table 4. *Classification performance of the Convolutional Neural Network evaluated on the* ***NewHandPD dataset***.

Activation function	*Computational time (s)*	*Accuracy (0-1)*	*Weighted average of precision (0-1)*	*Weighted average of recall (0-1)*	*Weighted average of F1-score (0-1)*
ReLU	540.81	0.75 (0.73-0.76)	0.76 (0.74-0.78)	0.75 (0.73-0.77)	0.76 (0.74-0.77)
Leaky ReLU	591.64	0.83 (0.82-0.84)	0.83 (0.81-0.84)	0.83 (0.81-0.84)	0.83 (0.81-0.84)
CReLU	928.91	0.92 (0.91-0.93)	0.93 (0.91-0.94)	0.92 (0.90-0.93)	0.92 (0.91-0.93)
Sigmoid	537.96	0.57 (0.53-0.59)	1.00 (0.73-1.00)	0.57 (0.54-0.59)	0.72 (0.69-0.75)
Tanh	541.33	0.94 (0.93-0.95)	0.94 (0.92-0.95)	0.94 (0.92-0.95)	0.94 (0.92-0.95)
Softmax	584.22	0.55 (0.51-0.57)	1.00 (0.73-1.00)	0.55 (0.52-0.57)	0.71 (0.68-0.74)
VLReLU	596.99	0.85 (0.83-0.86)	0.87 (0.85-0.89)	0.85 (0.83-0.87)	0.85 (0.84-0.88)
ELU	574.94	0.89 (0.88-0.90)	0.89 (0.87-0.90)	0.89 (0.87-0.91)	0.89 (0.87-0.90)
SELU	571.76	0.85 (0.83-0.86)	0.86 (0.84-0.88)	0.85 (0.83-0.87)	0.85 (0.84-0.87)
QReLU (This study)	3,407.02	0.83 (0.82-0.85)	0.83 (0.81-0.86)	0.83 (0.82-0.84)	0.83 (0.82-0.85)
m-QReLU (This study)	3,453.62	0.79 (0.78-0.81)	0.79 (0.77-0.82)	0.79 (0.78-0.80)	0.79 (0.78-0.81)

***Table 5**. Classification accuracy and reliability (sub-section 3.3) of the Convolutional Neural Network evaluated on the **Kaggle Spiral Drawings dataset**.*

Activation function	*Computational time (s)*	*Accuracy (0-1)*	*Weighted average of precision (0-1)*	*Weighted average of recall (0-1)*	*Weighted average of F1-score (0-1)*
ReLU	700.16	0.47 (0.45-0.49)	0.47 (0.45-0.49)	0.47 (0.45-0.49)	0.47 (0.45-0.49)
Leaky ReLU	762.75	0.53 (0.51-0.55)	0.54 (0.52-0.56)	0.53 (0.51-0.55)	0.54 (0.52-0.55)
CReLU	1,203.73	0.80 (0.79-0.83)	0.84 (0.82-0.85)	0.80 (0.78-0.83)	0.80 (0.79-0.83)
Sigmoid	707.94	0.50 (0.46-0.52)	1.00 (0.69-1.00)	0.50 (0.47-0.52)	0.67 (0.64-0.70)
Tanh	700.40	0.63 (0.61-0.65)	0.65 (0.63-0.68)	0.63 (0.60-0.65)	0.64 (0.61-0.66)
Softmax	790.07	0.63 (0.62-0.65)	0.64 (0.62-0.66)	0.63 (0.60-0.65)	0.63 (0.61-0.65)
VLReLU	759.44	0.67 (0.65-0.69)	0.67 (0.65-0.69)	0.67 (0.65-0.69)	0.67 (0.65-0.69)
ELU	734.69	0.50 (0.46-0.52)	0.50 (0.46-0.52)	0.50 (0.46-0.52)	0.50 (0.46-0.52)
SELU	759.05	0.67 (0.66-0.70)	0.70 (0.68-0.71)	0.67 (0.65-0.69)	0.67 (0.66-0.70)
QReLU (This study)	3,527.64	0.67 (0.66-0.69)	0.68 (0.66-0.70)	0.67 (0.65-0.69)	0.67 (0.66-0.69)
m-QReLU (This study)	3,540.10	0.73 (0.72-0.76)	0.74 (0.69-0.76)	0.73 (0.68-0.75)	0.70 (0.69-0.73)

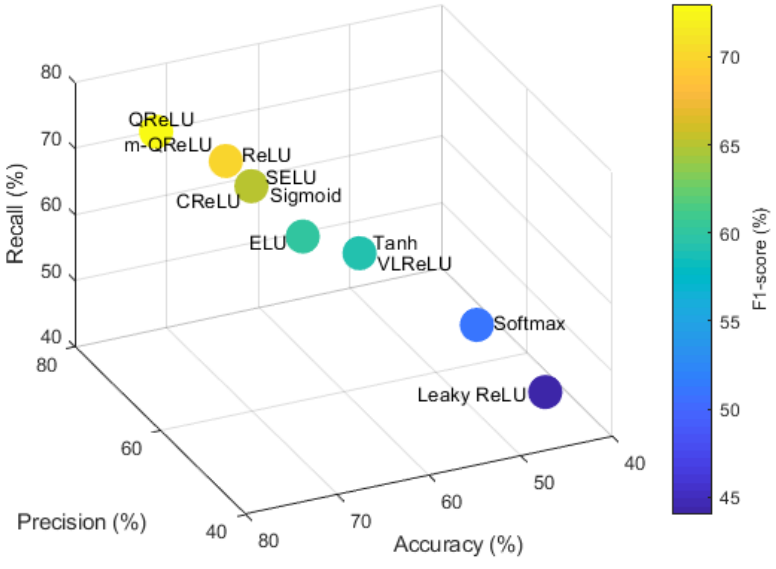

Figure 6. The classification accuracy and reliability (sub-section 3.3) of the Convolutional Neural Network on the ***COVID-19 Ultrasound dataset***, considering the main four metrics (sub-section 3.3) leveraged in percentages (%), i.e., accuracy, precision, recall, and F1-score. The activation functions (AFs) leading to the best classification are at the top-left corner of the plot (the novel QReLU and m-QReLU), whilst the one yielding the worst classification is at the bottom-right corner of it (Leaky ReLU). *Table A7* in the Appendix also includes the confidence intervals of such metrics for all AFs.

5 DISCUSSION

Further to an extensive review of existing ReLU AFs (sub-section 1.2), also considering that classical approaches have been unable to solve the 'dying ReLU' problem and taking into account the advantages of quantum states in AFs (listed in sub-section 1.3), two novel quantum-based AFs were mathematically formulated in sub-section 2.1 and developed in both TensorFlow and Keras (Parisi, 2020) to enable repeatability and reproducibility. Thus, the MNIST CNN-based classifier in TensorFlow, with two convolutional layers (**Fig. 4**) was selected to assess the impact of using either quantum AFs (QReLU and m-QReLU) on the classification accuracy and reliability (sub-section 3.3) on seven datasets as described in sub-section 2.1 and evaluated based on test ACC, precision, recall/sensitivity, and F1-score, as mentioned in sub-section 2.2.

The proposed QReLU leads to achieve the best classification accuracy and reliability (sub-section 3.3) on the MNIST benchmark dataset (ACC = 99%, F1-score = 99%, **Table A2** in the Appendix) to recognise handwritten digits serves as a regression test to validate the hypothesis whereby, using the CNN-based MNIST classifier, the highest classification accuracy and reliability (sub-section 3.3) are achieved with the presumed best AF. This hypothesis has been further confirmed by the m-QReLU achieving the second classification accuracy and reliability (ACC = 99%, F1-score = 99%, **Table A2** in the Appendix) across all eleven AFs evaluated as in sub-section 2.2. Achieving the same classification accuracy and reliability (sub-section 3.3) as the gold standard repeatable and reproducible AFs in CNNs (ReLU, the Leaky ReLU and the VLReLU) – readily available in both TensorFlow and Keras – the QReLU can be granted the designation of benchmark AF for the task of handwritten digits recognition performed on the MNIST benchmark dataset.

The benefits of avoiding the 'dying ReLU' problem became evident when assessing the same CNN architecture with the QReLU especially (ACC = 0.92/92%, F1-score = 0.93/93%, **Table A3** in the Appendix and **Fig. 5**), which achieved the best classification accuracy and reliability (sub-section 3.3) on critical image classification tasks, such as recognising PD-related patterns from spiral drawings in the 'Spiral HandPD' dataset. These improvements in both classification accuracy and F1-score are brought by leveraging superposition (section 2) that enables the proposed quantum activations to be more flexible regarding the choice of the most reliable solution derived to maximise classification accuracy and reliability (sub-section 3.3). The higher generalisability achieved via the two proposed quantum AFs in further support of the advantage of obviating the 'dying ReLU' issue is evident from the best classification accuracy and reliability (sub-section 3.3) in differentiating COVID-19 from both bacterial pneumonia and healthy controls from the Lung US data (**Table A7** in the Appendix and **Fig. 6** - QReLU and m-QReLU with ACC = 0.73/73% and F1-score = 0.73/73%). These increased accuracy and reliability (sub-section 3.3) due to entangled solutions from a quantum computational standpoint leads to overall higher diagnostic accuracy and reliability (sub-section 3.3), also empirically corroborated by the second-best classification outcomes attained on the second Lung US dataset (**Table A8** in the Appendix).

Whilst traditional ReLU approaches show highly variable classification outcomes, especially when they experience the 'dying ReLU' problem (**Table 5**, and **Tables A7 and A8** in the Appendix), both the QReLU and the m-QReLU were able to ensure a consistently higher classification accuracy and reliability (sub-section 3.3) across the entire variety of image classification tasks involved, from the benchmark handwritten digits recognition task (MNIST), to recognising PD-related patterns from spiral drawings taken from graphic tablets, and aiding detection of COVID-19 from bacteria pneumonia and healthy lungs based on US scans. The advantage of using the proposed AFs for COVID-19 detection lies in the potential value for their translational applications in a clinical setting, i.e., in leveraging CNNs with the QReLU or m-QReLU to detect COVID-19 in patients with neurodegenerative co-morbidities, such as PD, via non-ionising medical imaging (e.g., US). This added capability will come handy in future, as portable MRI and ML-enhanced MRI technologies will also become more affordable and widespread, thus being improvable with DL-based models (e.g., the CNN with QReLU or m-QReLU AFs in this study). Solutions either on edge devices or on the cloud for tele-diagnosis and tele-monitoring required in pandemics like the current one (COVID-19) could be soon suitable for in-home diagnostic and prognostic assessments too, which should improve personalised care for shielded or vulnerable individuals.

Moreover, competitive outcomes were obtained via the QReLU and the m-QReLU on three further datasets, e.g., 'NewHandPD dataset', the Kaggle and the UCI Spiral Drawings datasets, with ACC and F1-score mostly above 75% (**Tables 4 and 5**, and **Table A6** in the Appendix) using the CNN leveraged in this study (the MNIST CNN classifier). Such results also demonstrate the added capability of the proposed QReLU and the m-QReLU to avoid the vanishing gradient problem occurred using tanh (0% ACC and sensitivity/recall), as evaluated on the UCI Spiral Drawings dataset (**Table A6** in the Appendix).

Despite the overall increase in generalisability brought about by the QReLU and the m-QReLU, the computational cost of the CNN increased by four times as compared to the other nine AFs evaluated, except for the CReLU, against which a three-fold increase was reported (**Tables A2-A8** (Tables A2, A3, A6, A7, and A8 are in the Appendix)). Nevertheless, considering the importance of achieving higher classification accuracy and reliability (sub-section 3.3) over lower computational cost for diagnostic applications in a clinical setting, especially for the critical image classification tasks involved in this study, such as the detection of PD (**Tables A3-A6** (Tables A3 and A6 are in the Appendix)) and COVID-19 (**Tables A7** and **A8** in the Appendix), this increase in computational cost is not expected to impair the wide application of the two novel quantum AFs to aid such diagnostic tasks and any other medical applications involving image classification. However, such a higher computational cost will be more evident with deeper model architectures, thus potentially requiring optimisation of the trade-off between batch size and maximum number of epochs during training to achieve faster convergence for the use case and the size of the dataset of interest. This implies that, for deeper models, further technical assistance from ML engineers may be required. Furthermore, as the proposed quantum activation functions have not been evaluated yet on deeper neural networks than a CNN with four layers in total, nor on text data, it should be assessed whether exploding gradients can be avoided when increasing the size of the network;

if this issue occurred, deep Residual Networks (ResNet) (He *et al*., 2016) could be leveraged to mitigate it, as they display considerably lower gradients, thus helping to avoid the exploding gradient problem.

In fact, the QReLU and m-QReLU have been demonstrated as considerably better than the current (undisputedly assumed) gold standard AFs in CNNs, i.e., the traditional ReLU and the Leaky ReLU. An increase by 50-66% in both accuracy and reliability (sub-section 3.3) metrics was reported across both pattern recognition tasks, i.e., detection of PD-related patterns from spiral drawings (**Table 5**, and **Table A6** in the Appendix) and aiding diagnosis of COVID-19 from US scans (**Fig. 6** and **Table A7** in the Appendix). The two proposed quantum AFs also outperformed more cutting-edge ReLU AFs, such as the CReLU and the VLReLU, by 5-20% across all classification tasks considered, i.e., MNIST data classification (**Table A2** in the Appendix), spiral drawings PD-related pattern recognition (in particular, **Table 5**, and **Table A3** in the Appendix), and COVID-19 detection from US scans (**Fig. 6**, **Tables A7** and **A8** in the Appendix).

Moreover, the QReLU and the m-QReLU led the CNN MNIST classifier to achieve a comparable classification accuracy and reliability (sub-section 3.3) on the MNIST dataset as deeper CNNs, ranging from three to four layers (LeCun *et al.*, 1998; Siddique *et al.*, 2019; Ahlawat *et al.*, 2020), including deeper CNN architectures (Chen *et al.*, 2018). It is worth noting that, when leveraging the QReLU and the m-QReLU, the CNN with hyperparameters based on the MNIST data outperformed (ACC = 92%, F1-score = 93%, **Fig. 5**, and **Table A3** in the Appendix) deeper CNNs from published studies by over 2% (Pereira *et al.*, 2016c) in aiding the diagnosis of PD from patterns in spiral drawings (e.g., using the 'Spiral HandPD' data). The CNN model with either QReLU or m-QReLU as AFs achieved a comparable precision (**Fig. 6**, and **Table A7** in the Appendix) to the best-performing classifier on the COVID 19 Ultrasound dataset, i.e., the sixteen-layered POCOVID-Net CNN model (Born *et al.*, 2020).

These outcomes show that, by the avoidance of the 'dying ReLU' problem, using QReLU or m-QReLU can minimise the need for optimisation of CNN's hyperparameters and obviate the need for several convolutional layers in CNNs and any CNN-derived models, as demonstrated above and in section 4. The implications of the two above-mentioned practical benefits are multiple. Firstly, the two proposed AFs may also improve accuracy and reliability (sub-section 3.3) when considering image classification tasks that involve deeper architectures than the CNN used in this study. Thus, the proposed AFs may be viable alternatives to the ReLU AF, which is the current gold standard AF in CNNs. Second, by this improvement when deeper architectures may be required, the QReLU and m-QReLU may be suitable for tasks that require scalability of CNNs. Third, the proposed quantum AFs may enable more effective transfer learning, such as for COVID-19 detection in multiple geographical areas, as well as extending trained deep neural networks to further diagnostic tasks, including prognostic applications too. These benefits clearly outweigh the higher computational cost, which is not an issue for the target practical applications in healthcare, wherein early detection and diagnostic accuracy are key to improve clinical outcomes.

Overall, the avoidance of the 'dying ReLU' problem achieved via QReLU and m-QReLU is expected to radically shift the paradigm of blindly relying on the traditional ReLU AF in CNN and any CNN-derived models,

and embrace innovative approaches, including quantum-based, such as the two novel AFs designed, developed, and validated in this study.

6 CONCLUSIONS

The proposed QReLU and m-QReLU were proved to be the first two AFs in the recorded history of DL to avoid the 'dying ReLU' problem, via quantum computational approaches leveraging the principles of entanglement and superposition, by design. This was based on a thorough analysis of the classification accuracy and reliability (sub-section 3.3) of a CNN classifier leveraging the two quantum AFs developed in this study (QReLU and m-QReLU), and evaluated against nine AFs, including ReLU and its main recent repeatable and reproducible advances, as well as relevant published studies. The quantum computational algorithms describing the methodology and AF were implemented in TensorFlow and Keras. This added capability ensured accurate and reliable classification for recognising PD-related patterns from spiral drawings and detecting COVID-19 from non-ionising medical imaging (US) data. The results attained demonstrate that the long-standing 'dying ReLU' problem in the history of DL had to be solved not via ReLU-like classical approaches, but by a disruptive, innovative quantum-inspired computational paradigm, such as the one underpinning the two novel QReLU and m-QReLU activation functions.

Furthermore, their availability in both Google's TensorFlow and Keras – the two most widely used libraries in Python for DL - facilitate their wide application beyond clinical diagnostics, including medical prognostics and any other applications involving image classification. Thus, the QReLU and m-QReLU can aid detection of COVID-19 during these unprecedented times of this pandemic, as well as deliver continuous value added in aiding the diagnosis of PD based on pattern recognition from spiral drawings. Considering that the QReLU and m-QReLU were found to yield the most accurate and reliable results in presence of both binary and multi-class classification tasks, as new variants of COVID-19 are emerging as the virus mutates, the proposed quantum activations could be leveraged to help in identifying such variants and classifying them in a non-invasive and safe manner.

Noteworthily, when leveraging the proposed quantum AFs, the CNN model achieved comparable classification accuracy and reliability (sub-section 3.3) to deeper CNN and related architectures across all image recognition tasks involved in this study, from handwritten digits recognition to detection of PD-related patterns from spiral drawings and COVID-19 from lung US scans. These findings suggest that optimising the design of existing activation functions via novel paradigms in DL, such as quantum-inspired ones, has the potential of obviating the use of deeper models to achieve the required classification performance when dealing with medical images. The outcomes from this study corroborate the benefit of using AFs that avoid the 'dying ReLU' problem for critical image classification tasks, such as for medical diagnoses, making them a viable alternative to the current gold

standard AF in CNNs, i.e., the ReLU. This study is expected to have a radical impact in redefining the benchmark AFs in CNN and related architectures for applications across academic research and industry.

Future work will focus on demonstrating these improvements in performance brought by the QReLU and the m-QReLU to extend the use of such novel quantum activations to small clinics that have less computational resources than large hospitals, thus helping to improve clinical outcomes more broadly. Furthermore, as medical images are intrinsically noisy due to the artifacts generated during scanning procedures and by the imaging technique itself, future research will evaluate the proposed quantum activation functions in presence of noisy text data to improve their classification for health-related applications, e.g., sentiment analysis, and with other model architectures, such as recurrent neural networks.

ACKNOWLEDGMENTS

The authors would like to thank two research assistants from the University of Bradford, Ms Smriti Kotiyal and Mr Rohit Trivedi, for their assistance to the background review relevant for this paper.

The authors declare that no ethical approval was required for carrying out the study, as the data used in it were taken from publicly available repositories and appropriately referenced in text. Moreover, the authors declare that this was the result of a HEIF 2020 University of Bradford COVID-19 response-funded project ‘Quantum ReLU-based COVID-19 Detector: A Quantum Activation Function for Deep Learning to Improve Diagnostics and Prognostics of COVID-19 from Non-ionising Medical Imaging’. However, the funding source was not involved in conducting the study and/or preparing the article.

REFERENCES

Ahlawat, S., Choudhary, A., Nayyar, A., Singh, S., Yoon, B. (2020). Improved Handwritten Digit Recognition Using Convolutional Neural Networks (CNN). *Sensors*, 20(12), 3344.

Barabasi, I., Tappert, C. C., Evans, D., Leider, A. M. (2019). Quantum Computing and Deep Learning Working Together to Solve Optimization Problems. 2019 *International Conference on Computational Science and Computational Intelligence* (*CSCI*).

Beam, A. L., and Kohane, I. S. (2018). Big Data and Machine Learning in Health Care. *JAMA*, 319(13), 1317-1318.

Beauchamp, L. C., Finkelstein, D. I., Bush, A. I., Evans, A. H., Barnham, K. J. (2020). Parkinsonism as a Third Wave of the COVID-19 Pandemic? *Journal of Parkinson's Disease*, 1-11.

Bhaskar, S., Bradley, S., Israeli-Korn, S., B. M., Chattu, V. K., Thomas, P., Mart, S. (2020). Chronic Neurology in COVID-19 Era: Clinical Considerations and Recommendations from the REPROGRAM Consortium. *Frontiers in Neurology*.

Born, J., Brändle, G., Cossio, M., Disdier, M., Goulet, J., Roulin, J., Wiedemann, N. (2020). POCOVID-Net: automatic detection of COVID-19 from a new lung ultrasound imaging dataset (POCUS). *arXiv*:2004.12084.

Born, J. (2020). Automatic Detection of COVID-19 from Ultrasound Data. *GitHub repository*. Available at: https://github.com/jannisborn/covid19_ultrasound.

Campbell, S. A., Ruan, S., Wolkowicz, G., Wu, J. (1999). Stability and bifurcation of a simple neural network with multiple time delays. *Fields Institute Communications*, 21(4), 65-79.

Cao, Y., Guerreschi, G. G., Aspuru-Guzik, A. (2017). Quantum Neuron: an elementary building block for machine learning on quantum computers. *arXiv*:1711.11240.

Centers for Disease Control and Prevention. (2020). Retrieved on July 13th, 2020, from *Coronavirus disease*: https://www.cdc.gov/coronavirus/2019-ncov/symptoms-testing/symptoms.html.

Chen, F., Chen, N., Mao, H., Hu, H. (2018). Assessing four neural networks on handwritten digit recognition dataset (MNIST). *arXiv*:1811.08278.

Ciliberto, C., Herbster, M., Ialongo, A. D., Pontil, M., Rocchetto, A., Severini, S., Wossnig, L. (2018). Quantum machine learning: a classical perspective. *Proceedings of the Royal Society*, 474: 20170551.

Cleve, R., Ekert, A., Macchiavello, C., Mosca, M. (1998). Quantum algorithms revisited. *Proceedings of the Royal Society*, 454, 339–354.

Cong, I., Choi, S., Lukin, M. D. (2019). Quantum Convolutional Neural Networks. *Nature Physics*, 15, 1273–1278.

Cui, N., 2018. Applying Gradient Descent in Convolutional Neural Networks. *Journal of Physics: Conference Series*, 1004, p.012027.

Cui, J., Li, F., Shi, Z.-L. (2019). Origin and evolution of pathogenic coronaviruses. *Nature Reviews Microbiology*, 17, 181-192.

Gao, H., Cai, L., Ji, S. (2020). Adaptive Convolution ReLUs. *Thirty-Fourth AAAI Conference on Artificial Intelligence*.

Glorot, X., Bordes, A., Bengio, Y. (2011, June). Deep sparse rectifier neural networks. In *Proceedings of the Fourteenth International Conference on Artificial Intelligence and Statistics*, 315-323.

Gold, S., and Rangarajan, A. (1996). Softmax to softassign: Neural network algorithms for combinatorial optimization. *Journal of Artificial Neural Networks*, 2(4), 381-399.

Han, J., and Moraga, C. (1995, June). The influence of the sigmoid function parameters on the speed of backpropagation learning. In *International Workshop on Artificial Neural Networks*, 195-201. Springer, Berlin, Heidelberg.

Harrington, P. D. B. (1993). Sigmoid transfer functions in backpropagation neural networks. *Analytical Chemistry*, 65(15), 2167-2168.

He, K., Zhang, X., Ren, S., Sun, J. (2015). Delving Deep into Rectifiers: Surpassing Human-Level Performance on ImageNet Classification. *IEEE International Conference on Computer Vision (ICCV)*. Santiago.

He, K., Zhang, X., Ren, S., & Sun, J. (2016). Deep residual learning for image recognition. In *Proceedings of the IEEE Conference on Computer Vision and Pattern Recognition (CVPR)*, 770-778.

Hinton, G. E., and Salakhutdinov, R. R. (2006). Reducing the Dimensionality of Data with Neural Networks. *Science*, 504-507, 313.

Hripcsak, G., & Rothschild, A. S. (2005). Agreement, the F-measure, and reliability in information retrieval. *Journal of the American Medical Informatics Association*, *12*(3), 296-298.

Hu, W. (2018). Towards a Real Quantum Neuron. *Natural Science*, 10 (3).

Isenkul, M., Sakar, B., Kursun, O. (2014, May). Improved spiral test using digitized graphics tablet for monitoring Parkinson's disease. In *Proceedings of the International Conference on e-Health and Telemedicine*, 171-175.

Jozsa, R., and Linden, N. (2003). On the role of entanglement in quantum-computational speed-up. *Proceedings of the Royal Society*, 10.1098.

Ker, J., Wang, L., Rao, J., Lim, T. (2017). Deep Learning Applications in Medical Image Analysis. *IEEE Access*, 6: 9375 - 9389.

Klambauer, G., Unterthiner, T., & Mayr, A. (2017). Self-Normalizing Neural Networks. *arXiv*:1706.02515.

Kohavi, R. (1995). A study of cross-validation and bootstrap for accuracy estimation and model selection. In *IJCAI*, 14(2), 1137-1145.

Kollias, D., Tagaris, A., Stafylopatis, A., Kollias, S., Tagaris, G. (2018). Deep neural architectures for prediction in healthcare. *Complex & Intelligent Systems*, 4, 119-131.

Konarac, D., Bhattacharyya, S., Gandhia, T. K., Panigrahia, B. K. (2020). A Quantum-Inspired Self-Supervised Network model for automatic segmentation of brain MR images. *Applied Soft Computing*, 93, 106348.

Krizhevsky, A., Sutskever, I., Hinton, G. E. (2012). ImageNet Classification with Deep Convolutional Neural Networks. *Proceedings of the Advances in Neural Information Processing Systems*. 1097-1105.

LeCun, Y., and Bengio, Y. (1995). Convolutional networks for images, speech, and time-series. In M. A. Arbib (Ed.), The handbook of brain theory and neural networks. *MIT Press*.

LeCun, Y., Bottou, L., Bengio, Y., & Haffner, P. (1998). Gradient-based learning applied to document recognition. *Proceedings of the IEEE*, 86(11), 2278-2324.

LeCun, Y., Bengio, Y., Hinton, G. (2015). Deep Learning. *Nature*. 521. 436-44.

Liew, S. S., Khalil-Hani, M., Bakhteri, R. (2016). Bounded activation functions for enhanced training stability of deep neural networks on visual pattern recognition problems. *Neurocomputing*, 216, 718-734.

Litjens, G., Kooi, T., Bejnordi, B. E., Setio, A. A., Ciompi, F., Ghafoorian, M., Sánchez, C. I. (2017). A survey on deep learning in medical image analysis. *Medical Image Analysis, 42*, 60-88.

Maas, A. L., Hannun, A. Y., Ng, A. Y. (2013). Rectifier Nonlinearities Improve Neural Network Acoustic Models. *Proceedings of the 30th International Conference on Machine Learning*. Atlanta, Georgia, USA: JMLR: W&CP.

Macaluso, A., Clissa, L., Lodi, S., Sartori, C. (2020). A Variational Algorithm for Quantum Neural Networks. *ICCS 2020: Computational Science Lecture Notes in Computer Science*, 12142, 591-604. Springer.

Nair, V., and Hinton, G. (2010). Rectified Linear Units Improve Restricted Boltzmann Machines. *International Conference on Machine Learning (ICML)*, Omnipress, 807-814.

Nielsen, M. A., and Chuang, s. (2002). Quantum Computation and Quantum Information. *American Journal of Physics*, 70, 558.

Parisi, L. (2020). QReLU and m-QReLU in TensorFlow and Keras. *GitHub repository*. Available at: https://github.com/luca-parisi/QReLU_m-QReLU_TensorFlow_Keras.

Pedamonti, D. (2018). Comparison of non-linear activation functions for deep neural networks on MNIST classification task. *arXiv*:1804.02763.

Pereira, C. R., Pereira, D. R., Silva, F. A., Masieiro, J. P., Weber, S. A., Hook, C., Papa, J. P. (2016a). A new computer vision-based approach to aid the diagnosis of Parkinson's disease. *Computer Methods and Programs in Biomedicine*, *136*, 79-88.

Pereira, C. R., Weber, S. A., Hook, C., Rosa, G. H., Papa, J. P. (2016b). Deep learning-aided Parkinson's disease diagnosis from handwritten dynamics. In *2016 29th SIBGRAPI Conference on Graphics, Patterns, and Images (SIBGRAPI)*, 340-346. IEEE.

Pereira, C. R., Pereira, D. R., Papa, J. P., Rosa, G. H., Yang, X. S. (2016c). Convolutional neural networks applied for Parkinson's disease identification. In *Machine Learning for Health Informatics*, 377-390. Springer, Cham.

Qiu, S., Xu, X., Cai, B. (2018). FReLU: Flexible Rectified Linear Units for Improving Convolutional Neural Networks. *arXiv*:1706.08098v2.

Rumelhart, D. E., Hinton, G. E., Williams, R. J. (1986). Learning representations by back-propagating errors. *Nature*, 323, 533–536.

Russakovsky, O., Deng, J., Su, H., Krause, J., Satheesh, S., Ma, S., Fei-Fei, L. (2015). ImageNet Large Scale Visual Recognition Challenge. *International Journal of Computer Vision*, 115, 211-252.

Sakar, B. E., Isenkul, M. E., Sakar, C. O., Sertbas, A., Gurgen, F., Delil, S., Kursun, O. (2013). Collection and analysis of a Parkinson speech dataset with multiple types of sound recordings. *IEEE Journal of Biomedical and Health Informatics*, *17*(4), 828-834.

Schuld, M., Sinayskiy, I., Petruccione, F. (2014). The quest for a Quantum Neural Network. *Quantum Information Processing*, 13, 2567-2586.

Shang, W., Sohn, K., Almeida, D., Lee, H. (2016). Understanding and improving convolutional neural networks via concatenated rectified linear units. *Proceedings of the 33rd International Conference on Machine Learning, JMLR.* NY, USA: W&CP.

Shi, H., Han, X., Jiang, N., Cao, Y., Alwalid, O., Gu, J., Zheng, C. (2020). Radiological findings from 81 patients with COVID-19 pneumonia in Wuhan, China: a descriptive study. *Lancet*. Infectious diseases.

Siddique, F., Sakib, S., Siddique, M. A. B. (2019, September). Recognition of handwritten digit using convolutional neural network in python with tensorflow and comparison of performance for various hidden layers. In 2019 *5th International Conference on Advances in Electrical Engineering (ICAEE)* (pp. 541-546). IEEE.

Solenov, D., Brieler, J., Scherrer, J. F. (2018). The Potential of Quantum Computing and Machine Learning to Advance Clinical Research and Change the Practice of Medicine. *Missouri Medicine*, 115(5): 463–467.

TensorFlow (2020). Tf.Nn.Leaky_Relu | Tensorflow Core V2.3.0. Retrieved on February 10th, 2021, from https://www.tensorflow.org/api_docs/python/tf/nn/leaky_relu.

TensorFlow (2020). Tf.Keras.Layers.Leakyrelu | Tensorflow Core V2.3.0. Retrieved on February 10th, 2021, from https://www.tensorflow.org/api_docs/python/tf/keras/layers/LeakyReLU.

Verity, R., Okell, L. C., Dorigatti, I., Winskill, P., Whittaker, C., Imai, N., Cori, A. (2020). Estimates of the severity of coronavirus disease 2019: a model-based analysis. *Lancet*, 20 (6); 669-677.

WHO (Mar 2020). Retrieved on January 12th, 2021, from https://www.who.int/dg/speeches/detail/who-director-general-s-opening-remarks-at-the-media-briefing-on-covid-19---11-march-2020.

Xu, B., Wang, N., Chen, T., Li, M. (2015). Empirical evaluation of rectified activations in convolutional network. *arXiv*:1505.00853.

Zeiler, M. D., and Fergus, R. (2014). Visualizing and Understanding Convolutional Networks. *ECCV 2014: European Conference on Computer Vision*, 818-833.

Zham, P., Kumar, D. K., Dabnichki, P., Poosapadi Arjunan, S., Raghav, S. (2017). Distinguishing different stages of Parkinson's disease using composite index of speed and pen-pressure of sketching a spiral. *Frontiers in Neurology*, *8*, 435.

Zhou, F., Yu, T., Du, R., Fan, G., Liu, Y., Liu, Z., Cao, B. (2020). Clinical course and risk factors for mortality of adult inpatients with COVID-19 in Wuhan, China: a retrospective cohort study. *Lancet*, 395(10229), 1054-1062.

APPENDIX

Table A1 summarises the main activation functions commonly used in deep neural networks, including the convolutional neural network (CNN), with their equations and references.

Table A1. *The main activation functions used in deep neural networks, such as the convolutional neural network (CNN), with their equations and references.*

Activation function	**Equation**	**Reference**
Logistic Sigmoid	$f(x) = \frac{1}{1 + e^{-x}}$	Han & Moraga (1995)
tanh	$f(x) = tanh(x) = \frac{2}{1 + e^{-2x}} - 1$	Harrington (1993)
Softmax	$f_i(x) = \frac{e^{x_i}}{\sum_{j=1}^{J} e^{x_j}}, \quad \forall\, i = [1, J]$	Gold & Rangarajan (1996)
ArcTan	$f(x) = tan^{-1}(x)$	Campbell *et al.* (1999)
SoftPlus	$f(x) = ln(1 + e^{x})$	Glorot *et al.* (2011)
Rectified Linear Unit (ReLU)	$f(x) = \begin{cases} 0 \,\forall\, x < 0 \\ x \,\forall\, x \geq 0 \end{cases}$	Nair & Hinton (2010)
Leaky Rectified Linear Unit (LReLU)	$f(x) = \begin{cases} x \,\forall\, x > 0 \\ \alpha x \,\forall\, x \leq 0, \\ where\ \alpha = 0.01 \end{cases}$	Maas *et al.* (2013)
Parametric Rectified Linear Unit (PReLU)	$f(\alpha, x) = \begin{cases} \alpha x \,\forall\, x < 0 \\ x \,\forall\, x \geq 0 \end{cases}$	He *et al.* (2015)
Exponential Linear Unit (ELU)	$f(\alpha, x) = \begin{cases} x \,\forall\, x > 0 \\ \alpha(e^{x} - 1) \,\forall\, x \leq 0 \end{cases}$	Maas *et al.* (2013)
Scaled Exponential Linear Unit (SELU)	$f(\alpha, x) = \lambda \begin{cases} x \,\forall\, x \geq 0 \\ \alpha(e^{x} - 1) \,\forall\, x < 0, \\ where\ \lambda = 1.0507 \text{ and } \alpha = 1.67326 \end{cases}$	Maas *et al.* (2013)
Concatenated Rectified Linear Unit (CReLU)	$f(x) = +\big(ReLU(x), ReLU(-x)\big)$	Shang *et al.* (2016)
Flexible Rectified Linear Unit (FReLU)	$f(x) = \begin{cases} x + b_l \,\forall\, x > 0 \\ x \,\forall\, x \leq 0 \end{cases}$	Qiu *et al.* (2018)
Randomized Rectified Linear Unit (RReLU)	$f(x) = y_{ji} = \begin{cases} x_{ji} \,\forall\, x_{ji} \geq 0 \\ a_{ji} x_{ji} \,\forall\, x_{ji} < 0 \end{cases}$	Xu *et al.* (2015)

The following tables summarise the results on the evaluation of the CNN with different activation functions, including the novel QReLU and m-QReLU, across different datasets:

- **Table A2** on the MNIST dataset.
- **Tables A3 and A6** on the Spiral HandPD and University California Irvine (UCI) Spiral Drawings datasets.
- **Tables A7 and A8** on the COVID-19 Ultrasound and POCUS 19 datasets.

***Table A2**. Classification accuracy and reliability (sub-section 3.3) of the Convolutional Neural Network evaluated on the **MNIST dataset**.*

Activation function	*Computational time (s)*	*Accuracy (0-1)*	*Weighted average of precision (0-1)*	*Weighted average of recall (0-1)*	*Weighted average of F1-score (0-1)*
ReLU	725.79	0.99 (0.98-1.00)	0.99 (0.99-1.00)	0.99 (0.98-1.00)	0.99 (0.98-0.99)
Leaky ReLU	773.84	0.99 (0.98-1.00)	0.99 (0.99-1.00)	0.99 (0.98-1.00)	0.99 (0.98-0.99)
CReLU	1,214.08	0.98 (0.98-0.99)	0.98 (0.98-0.99)	0.98 (0.98-0.99)	0.98 (0.98-0.99)
Sigmoid	722.50	0.98 (0.95-0.99)	0.98 (0.96-0.99)	0.98 (0.96-0.99)	0.98 (0.96-0.99)
Tanh	725.51	0.98 (0.97-0.99)	0.98 (0.98-0.99)	0.98 (0.98-0.99)	0.98 (0.98-0.99)
Softmax	865.03	0.98 (0.97-0.99)	0.98 (0.98-0.99)	0.98 (0.98-0.99)	0.98 (0.98-0.99)
VLReLU	794.36	0.99 (0.98-1.00)	0.99 (0.99-1.00)	0.99 (0.98-1.00)	0.99 (0.98-0.99)
ELU	767.45	0.98 (0.97-0.99)	0.98 (0.98-0.99)	0.98 (0.98-0.99)	0.98 (0.98-0.99)
SELU	771.69	0.98 (0.98-0.99)	0.98 (0.98-0.99)	0.98 (0.98-0.99)	0.98 (0.98-0.99)
QReLU** **(This study)	3,369.73	0.99 (0.99-1.00)	0.99 (0.99-1.00)	0.99 (0.99-1.00)	0.99 (0.99-1.00)
m-QReLU** **(This study)	3,643.50	0.98 (0.98-0.99)	0.98 (0.98-0.99)	0.98 (0.98-0.99)	0.98 (0.98-0.99)

***Table A3**. Classification accuracy and reliability (sub-section 3.3) of the Convolutional Neural Network evaluated on the **Spiral HandPD dataset**.*

Activation function	*Batch size*	*Number of epochs*	*Computational time (s)*	*Accuracy (0-1)*	*Weighted average of precision (0-1)*	*Weighted average of recall (0-1)*	*Weighted average of F1-score (0-1)*	*ROC-AUC (0-1)*
ReLU	128	2,000	709.86	0.81 (0.76-0.87)	1.00 (0.98-1.00)	0.81 (0.78-0.83)	0.90 (0.85-0.93)	0.83 (0.80-0.85)
ReLU	128	1,500	527.25	0.81 (0.76-0.87)	0.87 (0.85-0.89)	0.81 (0.78-0.83)	0.83 (0.79-0.84)	0.82 (0.79-0.85)
ReLU	64	2,000	375.41	0.78 (0.74-0.81)	0.78 (0.74-0.81)	0.78 (0.74-0.81)	0.78 (0.74-0.81)	0.77 (0.72-0.80)
Leaky ReLU	128	2,000	783.76	0.82 (0.79-0.85)	0.83 (0.81-0.85)	0.82 (0.79-0.84)	0.83 (0.80-0.84)	0.81 (0.77-0.83)
Leaky ReLU	128	1,500	550.40	0.82 (0.79-0.85)	0.86 (0.83-0.88)	0.82 (0.79-0.85)	0.84 (0.82-0.86)	0.83 (0.79-0.84)
Leaky ReLU	64	2,000	405.47	0.74 (0.72-0.76)	0.79 (0.77-0.82)	0.74 (0.72-0.76)	0.76 (0.72-0.78)	0.78 (0.74-0.81)
CReLU	128	2,000	1,226.09	0.89 (0.87-0.92)	0.95 (0.93-0.96)	0.89 (0.87-0.91)	0.91 (0.88-0.92)	0.92 (0.88-0.94)
CReLU	128	1,500	917.78	0.85 (0.82-0.87)	0.93 (0.91-0.95)	0.85 (0.82-0.87)	0.88 (0.87-0.90)	0.88 (0.87-0.90)
CReLU	64	2,000	642.39	0.88 (0.87-0.90)	0.87 (0.85-0.89)	0.88 (0.87-0.90)	0.87 (0.85-0.89)	0.87 (0.85-0.89)
Sigmoid	128	2,000	717.86	0.85 (0.80-0.88)	0.88 (0.85-0.90)	0.85 (0.82-0.87)	0.86 (0.83-0.88)	0.86 (0.82-0.88)
Sigmoid	128	1,500	537.45	0.78 (0.74-0.81)	0.80 (0.77-0.84)	0.78 (0.74-0.81)	0.79 (0.78-0.81)	0.78 (0.74-0.81)
Sigmoid	64	2,000	374.21	0.80 (0.77-0.84)	1.00 (0.98-1.00)	0.80 (0.77-0.84)	0.90 (0.88-0.92)	0.83 (0.79-0.84)
Tanh	128	2,000	712.78	0.82 (0.81-0.85)	0.92 (0.90-0.94)	0.82 (0.79-0.84)	0.86 (0.82-0.88)	0.83 (0.79-0.84)
Tanh	128	1,500	546.08	0.80 (0.77-0.84)	0.83 (0.81-0.85)	0.80 (0.77-0.84)	0.81 (0.78-0.83)	0.81 (0.78-0.83)
Tanh	64	2,000	384.70	0.88 (0.87-0.90)	0.91 (0.89-0.92)	0.88 (0.79-0.84)	0.89 (0.87-0.91)	0.86 (0.83-0.88)
Softmax	128	2,000	799.64	0.85 (0.82-0.87)	0.84 (0.82-0.86)	0.85 (0.82-0.87)	0.84 (0.83-0.86)	0.84 (0.81-0.85)
Softmax	128	1,500	609.00	0.80 (0.77-0.84)	0.80 (0.77-0.84)	0.80 (0.77-0.84)	0.80 (0.77-0.84)	0.76 (0.72-0.78
Softmax	64	2,000	424.34	0.68 (0.64-0.72)	0.68 (0.64-0.72)	0.68 (0.64-0.72)	0.68 (0.64-0.72)	0.67 (0.62-0.70)
VLReLU	128	2,000	771.20	0.81 (0.79-0.84)	0.84 (0.82-0.86)	0.81 (0.78-0.83)	0.82 (0.80-0.84)	0.82 (0.80-0.83)
VLReLU	128	1,500	555.52	0.86 (0.83-0.88)	0.89 (0.87-0.91)	0.86 (0.83-0.88)	0.88 (0.79-0.84)	0.86 (0.83-0.88)
VLReLU	64	2,000	391.50	0.82 (0.79-0.85)	0.84 (0.82-0.86)	0.82 (0.79-0.85)	0.83 (0.81-0.85)	0.83 (0.81-0.85)
ELU	128	2,000	743.69	0.86 (0.84-0.88)	0.93 (0.91-0.94)	0.86 (0.83-0.88)	0.89 (0.86-0.91)	0.88 (0.85-0.90)
ELU	128	1,500	569.37	0.77 (0.72-0.80)	0.89 (0.87-0.91)	0.77 (0.72-0.80)	0.81 (0.78-0.83)	0.82 (0.79-0.85)
ELU	64	2,000	396.81	0.78 (0.74-0.81)	0.76 (0.72-0.78)	0.78 (0.74-0.81)	0.77 (0.72-0.80)	0.77 (0.72-0.80)
SELU	128	2,000	759.33	0.85 (0.80-0.88)	0.88 (0.85-0.90)	0.85 (0.82-0.87)	0.86 (0.83-0.88)	0.87 (0.85-0.88)
SELU	128	1,500	572.40	0.78 (0.76-0.80)	0.80 (0.77-0.84)	0.78 (0.76-0.80)	0.79 (0.78-0.81)	0.79 (0.77-0.82)
SELU	64	2,000	400.70	0.82 (0.79-0.84)	0.87 (0.85-0.89)	0.82 (0.79-0.84)	0.84 (0.82-0.86)	0.83 (0.81-0.85)
***QReLU** (This study)*	128	2,000	3,319.93	0.88 (0.87-0.90)	0.95 (0.93-0.97)	0.88 (0.87-0.90)	0.90 (0.88-0.92)	0.92 (0.91-0.95)
***QReLU** (This study)*	128	1,500	2735.29	0.82 (0.79-0.84)	0.92 (0.90-0.95)	0.82 (0.79-0.84)	0.85 (0.82-0.87)	0.89 (0.87-0.91)
QReLU	64	2,000	1895.47	0.88	0.94	0.88	0.90	0.92

(This study)				(0.87-0.90)	(0.93-0.96)	(0.87-0.90)	(0.88-0.92)	(0.90-0.94)
m-QReLU ***(This study)***	128	2,000	3,393.56	0.92 (0.90-0.95)	0.95 (0.94-0.96)	0.92 (0.90-0.94)	0.93 (0.91-0.95)	0.94 (0.93-0.96)
m-QReLU ***(This study)***	128	1,500	2819.78	0.91 (0.89-0.92)	0.94 (0.93-0.96)	0.91 (0.89-0.92)	0.92 (0.90-0.94)	0.92 (0.91-0.95)
m-QReLU ***(This study)***	64	2,000	1889.89	0.91 (0.89-0.92)	0.95 (0.94-0.96)	0.91 (0.89-0.92)	0.92 (0.90-0.94)	0.92 (0.93-0.96)

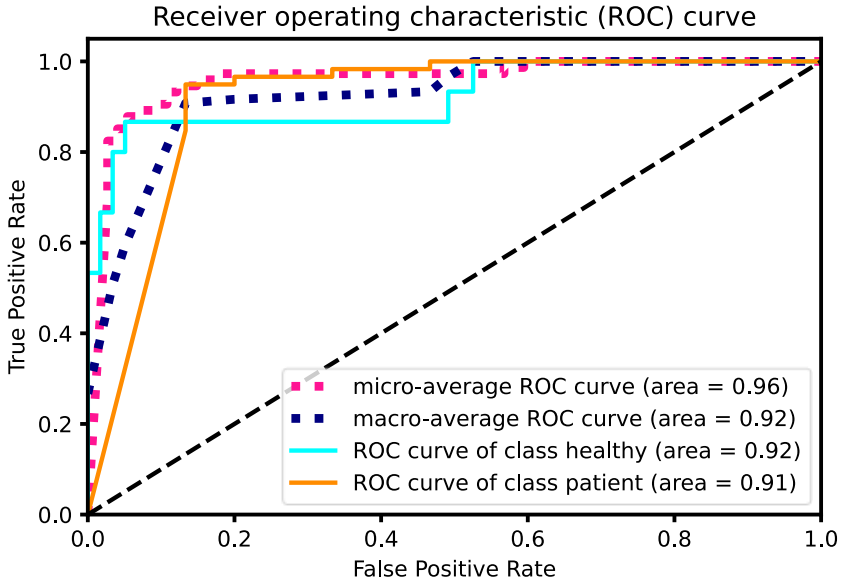

Figure 7A. The area under the receiver operating characteristic (ROC) curve of the Convolutional Neural Network (batch size = 64, number of epochs = 2,000) leveraging the m-QReLU activation function to classify the ***Spiral HandPD dataset***. The macro-average of the area under the curve (ROC-AUC) is equal to 0.92, as reported in the last row of *Table 3* in the Appendix.

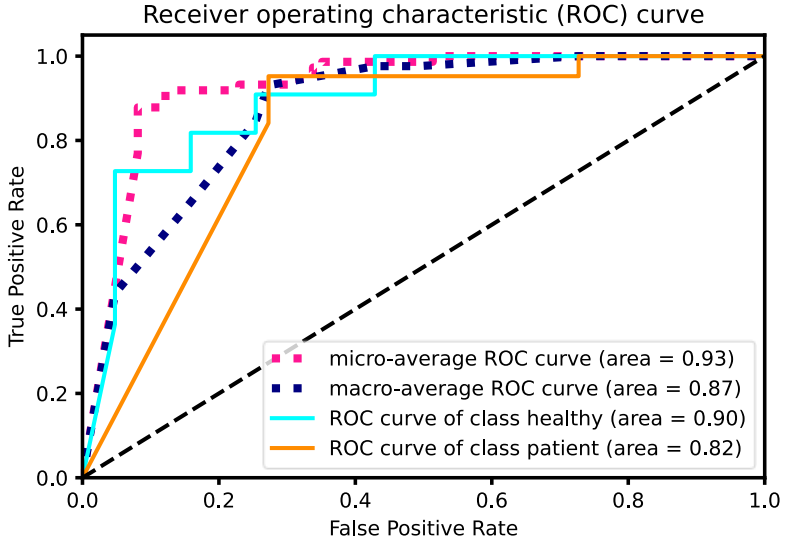

Figure 8A. The area under the receiver operating characteristic (ROC) curve of the Convolutional Neural Network (batch size = 64, number of epochs = 2,000) leveraging the CReLU activation function to classify the ***Spiral HandPD dataset***. The macro-average of the area under the curve (ROC-AUC) is equal to 0.87, as reported in the last row of *Table 3* in the Appendix.

Table A6*. Classification accuracy and reliability (sub-section 3.3) of the Convolutional Neural Network evaluated on the* ***University California Irvine (UCI) Spiral Drawings dataset****.*

Activation function	*Computational time (s)*	*Accuracy (0-1)*	*Weighted average of precision (0-1)*	*Weighted average of recall (0-1)*	*Weighted average of F1-score (0-1)*
ReLU	536.19	0.78 (0.74-0.81)	0.61 (0.59-0.64)	0.78 (0.75-0.81)	0.68 (0.64-0.72)
Leaky ReLU	595.66	0.76 (0.72-0.78)	0.58 (0.55-0.62)	0.76 (0.73-0.80)	0.66 (0.64-0.70)
CReLU	930.60	0.96 (0.95-0.97)	0.92 (0.91-0.94)	0.96 (0.95-0.97)	0.94 (0.92-0.95)
Sigmoid	543.40	1.00 (0.99-1.00)	1.00 (0.99-1.00)	1.00 (0.99-1.00)	1.00 (0.99-1.00)
Tanh	528.71	0.00 (0.00-0.02)	0.00 (0.00-0.02)	0.00 (0.00-0.03)	0.00 (0.00-0.02)
Softmax	585.93	1.00 (0.99-1.00)	1.00 (0.99-1.00)	1.00 (0.99-1.00)	1.00 (0.99-1.00)
VLReLU	751.23	0.86 (0.83-0.88)	0.74 (0.72-0.76)	0.86 (0.84-0.88)	0.80 (0.74-0.82)
ELU	734.46	0.52 (0.36-0.54)	0.27 (0.24-0.29)	0.52 (0.35-0.54)	0.36 (0.26-0.43)
SELU	730.00	0.62 (0.45-0.64)	0.38 (0.34-0.42)	0.62 (0.46-0.64)	0.47 (0.39-0.56)
QReLU ***(This study)***	3,449.55	0.82 (0.79-0.84)	0.67 (0.65-0.70)	0.82 (0.78-0.84)	0.74 (0.68-0.77)
m-QReLU ***(This study)***	3,325.67	0.78 (0.75-0.81)	0.61 (0.60-0.65)	0.78 (0.76-0.81)	0.68 (0.66-0.74)

Table A7*. Classification accuracy and reliability (sub-section 3.3) of the Convolutional Neural Network evaluated on the* ***COVID-19 Ultrasound dataset****.*

Activation function	***Batch size***	***Number of epochs***	***Computational time (s)***	***Accuracy (0-1)***	***Weighted average of precision (0-1)***	***Weighted average of recall (0-1)***	***Weighted average of F1-score (0-1)***	***ROC-AUC (0-1)***
ReLU	128	2,000	739.97	0.64 (0.62-0.67)	0.79 (0.77-0.82)	0.64 (0.62-0.66)	0.70 (0.64-0.73)	0.69 (0.67-0.72)
ReLU	128	1,500	524.79	0.67 (0.63-0.69)	0.67 (0.63-0.69)	0.67 (0.63-0.69)	0.67 (0.63-0.69)	0.66 (0.64-0.68)
ReLU	64	2,000	372.80	0.50 (0.48-0.52)	0.53 (0.50-0.55)	0.50 (0.48-0.52)	0.50 (0.48-0.52)	0.50 (0.48-0.52)
Leaky ReLU	128	2,000	799.42	0.45 (0.42-0.48)	0.45 (0.42-0.47)	0.45 (0.43-0.46)	0.44 (0.42-0.46)	0.45 (0.42-0.47)
Leaky ReLU	128	1,500	540.79	0.50 (0.48-0.52)	0.53 (0.50-0.55)	0.50 (0.48-0.52)	0.50 (0.48-0.52)	0.50 (0.48-0.52)
Leaky ReLU	64	2,000	380.67	0.83 (0.82-0.86)	0.92 (0.89-0.95)	0.83 (0.82-0.86)	0.85 (0.84-0.88)	0.86 (0.85-0.87)
CReLU	128	2,000	1,290.60	0.64 (0.62-0.67)	0.73 (0.70-0.76)	0.64 (0.62-0.66)	0.68 (0.65-0.71)	0.66 (0.64-0.68)
CReLU	128	1,500	589.89	0.67 (0.63-0.69)	0.75 (0.73-0.77)	0.67 (0.63-0.69)	0.67 (0.63-0.69)	0.68 (0.65-0.71)
CReLU	64	2,000	422.46	0.83 (0.82-0.86)	0.92 (0.89-0.95)	0.83 (0.82-0.86)	0.85 (0.84-0.88)	0.84 (0.83-0.87)
Sigmoid	128	2,000	737.86	0.64 (0.62-0.67)	0.73 (0.70-0.76)	0.64 (0.62-0.66)	0.66 (0.64-0.69)	0.67 (0.63-0.69)
Sigmoid	128	1,500	603.91	0.50 (0.48-0.52)	0.69 (0.67-0.72)	0.50 (0.48-0.52)	0.49 (0.47-0.51)	0.52 (0.50-0.54)
Sigmoid	64	2,000	442.30	0.50 (0.48-0.52)	0.61 (0.57-0.65)	0.50 (0.48-0.52)	0.52 (0.50-0.54)	0.51 (0.47-0.56)
Tanh	128	2,000	736.93	0.55 (0.52-0.58)	0.67 (0.63-0.69)	0.55 (0.53-0.58)	0.59 (0.56-0.62)	0.57 (0.52-0.61)
Tanh	128	1,500	584.12	0.83 (0.82-0.86)	0.89 (0.86-0.92)	0.83 (0.82-0.86)	0.83 (0.82-0.86)	0.84 (0.83-0.87)
Tanh	64	2,000	419.45	0.67 (0.63-0.69)	0.89 (0.86-0.92)	0.67 (0.63-0.69)	0.69 (0.67-0.72)	0.72 (0.70-0.74)
Softmax	128	2,000	841.28	0.45 (0.42-0.49)	0.61 (0.57-0.65)	0.45 (0.43-0.47)	0.51 (0.47-0.56)	0.54 (0.52-0.56)
Softmax	128	1,500	637.03	0.67 (0.63-0.69)	0.67 (0.63-0.69)	0.67 (0.63-0.69)	0.67 (0.63-0.69)	0.66 (0.64-0.68)
Softmax	64	2,000	442.71	0.67 (0.63-0.69)	0.89 (0.86-0.92)	0.67 (0.63-0.69)	0.67 (0.63-0.69)	0.70 (0.68-0.74)
VLReLU	128	2,000	780.88	0.55 (0.52-0.58)	0.67 (0.63-0.69)	0.55 (0.53-0.58)	0.59 (0.56-0.62)	0.57 (0.52-0.61)
VLReLU	128	1,500	586.19	0.50 (0.48-0.52)	0.83 (0.82-0.86)	0.50 (0.48-0.52)	0.58 (0.57-0.61)	0.53 (0.50-0.55)
VLReLU	64	2,000	404.4	0.67 (0.63-0.69)	0.89 (0.86-0.92)	0.67 (0.63-0.69)	0.71 (0.68-0.73)	0.72 (0.70-0.74)
ELU	128	2,000	760.62	0.64 (0.62-0.67)	0.61 (0.58-0.65)	0.64 (0.62-0.66)	0.60 (0.57-0.63)	0.62 (0.60-0.65)
ELU	128	1,500	582.56	0.83 (0.82-0.86)	0.89 (0.86-0.92)	0.83 (0.82-0.86)	0.83 (0.82-0.86)	0.84 (0.83-0.87)
ELU	64	2,000	414.95	0.67 (0.63-0.69)	0.89 (0.86-0.92)	0.67 (0.63-0.69)	0.67 (0.63-0.69)	0.71 (0.68-0.73)
SELU	128	2,000	758.67	0.64 (0.62-0.67)	0.73 (0.70-0.76)	0.64 (0.62-0.66)	0.65 (0.63-0.68)	0.67 (0.63-0.69)
SELU	128	1,500	578.19	0.67 (0.63-0.69)	0.75 (0.73-0.77)	0.67 (0.63-0.69)	0.67 (0.63-0.69)	0.70 (0.64-0.73)
SELU	64	2,000	406.37	0.50 (0.48-0.52)	0.69 (0.67-0.72)	0.50 (0.48-0.52)	0.49 (0.47-0.51)	0.53 (0.50-0.55)
QReLU ***(This study)***	128	2,000	3,429.00	0.73 (0.72-0.76)	0.76 (0.74-0.78)	0.73 (0.71-0.75)	0.73 (0.72-0.76)	0.75 (0.73-0.77)
QReLU	128	1,500	2,630.07	0.83	0.92	0.83	0.85	0.84

(This study)				(0.82-0.86)	(0.89-0.95)	(0.82-0.86)	(0.84-0.88)	(0.83-0.87)
QReLU ***(This study)***	64	2,000	774.05	0.83 (0.82-0.86)	0.89 (0.86-0.92)	0.83 (0.82-0.86)	0.83 (0.82-0.86)	0.84 (0.83-0.87)
m-QReLU ***(This study)***	128	2,000	3,465.98	0.73 (0.72-0.76)	0.76 (0.74-0.78)	0.73 (0.71-0.75)	0.73 (0.72-0.76)	0.88 (0.85-0.90)
m-QReLU ***(This study)***	128	1,500	2,270.96	0.83 (0.82-0.86)	0.89 (0.86-0.92)	0.83 (0.82-0.86)	0.83 (0.82-0.86)	0.84 (0.83-0.87)
m-QReLU ***(This study)***	64	2,000	755.74	0.83 (0.82-0.86)	0.92 (0.89-0.95)	0.83 (0.82-0.86)	0.85 (0.84-0.88)	0.84 (0.83-0.87)

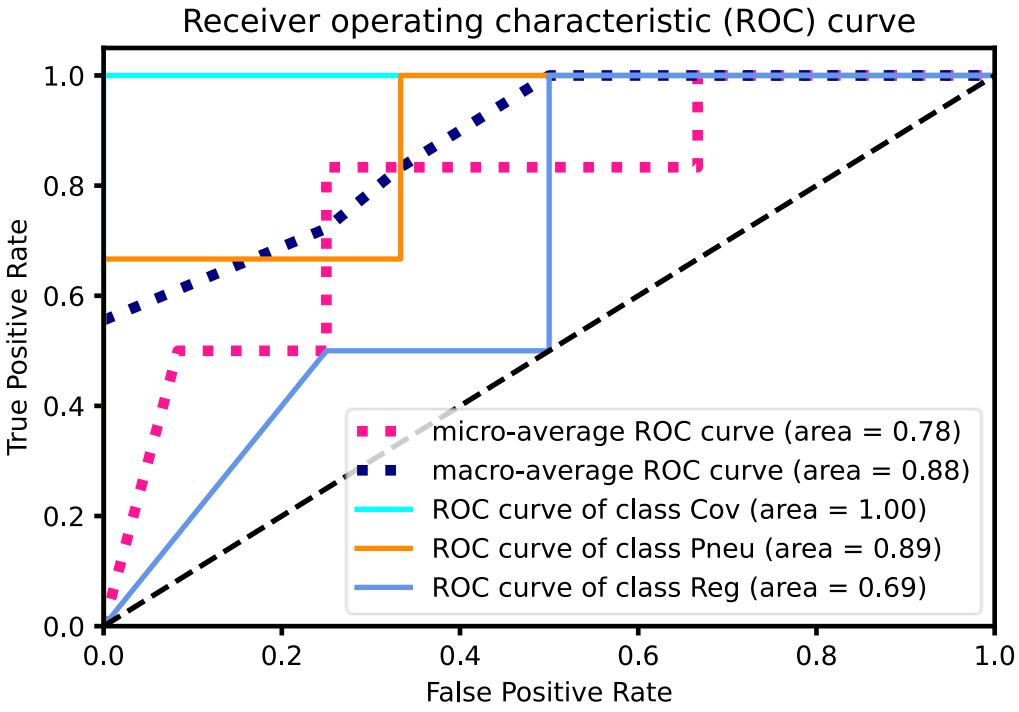

Figure 9A. The area under the receiver operating characteristic (ROC) curve of the Convolutional Neural Network (batch size = 128, number of epochs = 2,000) leveraging the m-QReLU activation function to classify the ***COVID-19 Ultrasound dataset***. The macro-average of the area under the curve (ROC-AUC) is equal to 0.88, as reported in *Table 3* in the Appendix.

***Table A8**. Classification accuracy and reliability (sub-section 3.3) of the Convolutional Neural Network, trained on the COVID-19 Ultrasound dataset (from Table 4), and evaluated on the **POCUS 19 dataset**.*

Activation function	*Computational time (s)*	*Accuracy (0-1)*	*Weighted average of precision (0-1)*	*Weighted average of recall (0-1)*	*Weighted average of F1-score (0-1)*
ReLU	720.63	0.40 (0.33-0.47)	1.00 (0.74-1.00)	0.40 (0.35-0.44)	0.57 (0.52-0.61)
Leaky ReLU	781.64	0.40 (0.32-0.46)	0.80 (0.77-0.84)	0.40 (0.35-0.44)	0.53 (0.47-0.57)
CReLU	1,229.20	0.60 (0.59-0.62)	0.87 (0.85-0.89)	0.60 (0.58-0.63)	0.63 (0.61-0.67)
Sigmoid	733.05	0.40 (0.33-0.47)	1.00 (0.74-1.00)	0.40 (0.35-0.44)	0.57 (0.52-0.61)
Tanh	730.13	0.40 (0.33-0.47)	1.00 (0.74-1.00)	0.40 (0.35-0.44)	0.57 (0.52-0.61)
Softmax	825.47	0.60 (0.59-0.62)	0.87 (0.85-0.89)	0.60 (0.58-0.63)	0.63 (0.61-0.67)
VLReLU	781.89	0.40 (0.32-0.46)	0.80 (0.77-0.84)	0.40 (0.35-0.44)	0.53 (0.47-0.57)
ELU	765.93	0.40 (0.33-0.47)	1.00 (0.74-1.00)	0.40 (0.35-0.44)	0.57 (0.52-0.61)
SELU	766.93	0.80 (0.77-0.84)	0.87 (0.85-0.89)	0.80 (0.78-0.84)	0.80 (0.76-0.83)
QReLU** **(This study)	3,407.86	0.60 (0.59-0.62)	0.87 (0.85-0.89)	0.60 (0.58-0.63)	0.63 (0.61-0.67)
m-QReLU** **(This study)	3,196.74	0.60 (0.59-0.62)	0.87 (0.85-0.89)	0.60 (0.58-0.63)	0.63 (0.61-0.67)